MNRAS **460,** 1500–1518 (2016)
Advance Access publication 2016 May 1
doi:10.1093/mnras/stw1031

The continuing story of SN IIb 2013df: new optical and IR observations and analysis

Tamás Szalai,[1⋆] József Vinkó,[1,2] Andrea P. Nagy,[1] Jeffrey M. Silverman,[2†] J. Craig Wheeler,[2] Govinda Dhungana,[3] G. Howie Marion,[2] Robert Kehoe,[3] Ori D. Fox,[4,5] Krisztián Sárneczky,[6,7] Gábor Marschalkó,[6,8] Barna I. Bíró,[8] Tamás Borkovits,[7,8] Tibor Hegedüs,[8] Róbert Szakáts,[6] Farley V. Ferrante,[3] Evelin Bányai,[6,9] Gabriella Hodosán,[6,10] János Kelemen[6] and András Pál[6]

[1]*Department of Optics and Quantum Electronics, University of Szeged, H-6720 Szeged, Dóm tér 9., Hungary*
[2]*Department of Astronomy, University of Texas at Austin, Austin, TX 78712-1205, USA*
[3]*Department of Physics, Southern Methodist University, Dallas, TX 75275, USA*
[4]*Department of Astronomy, University of California, Berkeley, CA 94720-3411, USA*
[5]*Space Telescope Science Institute, 3700 San Martin Drive, Baltimore, MD 21218, USA*
[6]*Konkoly Observatory, Research Centre for Astronomy and Earth Sciences, Hungarian Academy of Sciences, Konkoly Thege Miklós út 15-17, H-1121 Budapest, Hungary*
[7]*ELTE Gothard-Lendület Research Group, H-9700 Szombathely, Szent Imre herceg út 112, Hungary*
[8]*Baja Astronomical Observatory of University of Szeged, H-6500 Baja, Szegedi út, Kt. 766, Hungary*
[9]*Department of Physics of Complex Systems, Loránd Eötvös University, Pázmány P. sétány 1/A, H-1117 Budapest, Hungary*
[10]*School of Physics & Astronomy, University of St Andrews, St Andrews KY16 9SS, UK*

Accepted 2016 April 28. Received 2016 April 27; in original form 2016 February 24

ABSTRACT

SN 2013df is a nearby Type IIb supernova that seems to be the spectroscopic twin of the well-known SN 1993J. Previous studies revealed many, but not all interesting properties of this event. Our goal was to add new understanding of both the early- and late-time phases of SN 2013df. Our spectral analysis is based on six optical spectra obtained with the 9.2 m Hobby–Eberly Telescope during the first month after explosion, complemented by a near-infrared spectrum. We applied the SYNAPPS spectral synthesis code to constrain the chemical composition and physical properties of the ejecta. A principal result is the identification of 'high-velocity' He I lines in the early spectra of SN 2013df, manifest as the blue component of the double-troughed profile at ∼5650 Å. This finding, together with the lack of clear separation of H and He lines in velocity space, indicates that both H and He features form at the outer envelope during the early phases. We also obtained ground-based *BVRI* and $g'r'i'z'$ photometric data up to +45 d and unfiltered measurements with the ROTSE-IIIb telescope up to +168 d. From the modelling of the early-time quasi-bolometric light curve, we find $M_{\rm ej} \sim 3.2$–$4.6\ {\rm M}_{\odot}$ and $E_{\rm kin} \sim 2.6$–2.8×10^{51} erg for the initial ejecta mass and the initial kinetic energy, respectively, which agree well with the values derived from the separate modelling of the light-curve tail. Late-time mid-infrared excess indicates circumstellar interaction starting ∼1 yr after explosion, in accordance with previously published optical, X-ray, and radio data.

Key words: supernovae: general – supernovae: individual: SN 2013df.

1 INTRODUCTION

Type IIb supernovae (SN IIb) are thought to arise from the core-collapse of massive ($M > 8\ {\rm M}_{\odot}$) stars that lost most, but not all, of their thick H envelopes prior to explosion. This explains the special spectral evolution characteristic of the IIb subtype. The most conspicuous features are H Balmer lines that are strong around maximum light but weaken relatively quickly after that and He lines that become strong after the maximum. This makes SN IIb members of an intermediate group between Type II and the hydrogen-poor, stripped envelope Type Ib/c explosions. The first identified case of the subtype was SN 1987K (Filippenko 1988), while the best known member of the group is one of the closest and brightest SN of recent decades, SN 1993J (see e.g. Filippenko, Matheson &

⋆E-mail: szaszi@titan.physx.u-szeged.hu
† NSF Astronomy and Astrophysics Postdoctoral Fellow.

Ho 1993; Wheeler et al. 1993; Richmond et al. 1994; Barbon et al. 1995; Matheson et al. 2000).

While SN IIb constitute approximately 10–12 per cent of all core-collapse SNe (Li et al. 2011), detailed analyses have been published only on about a dozen of them. As from every type of supernovae, one of the main questions is the nature of the progenitor stars. Direct identification of the progenitor has been possible only in four cases: SN 1993J (a K-type supergiant with initial mass $M_{\rm in} \sim$ 13–22 $M_{\odot}$, which may be a component of an interacting binary system, see e.g. Van Dyk et al. 2002; Maund et al. 2004; Maund & Smartt 2009; Fox et al. 2014), SN 2008ax (a Wolf–Rayet star with $M_{\rm in} \sim$ 10–28 $M_{\odot}$, probably exploded in a binary system; Crockett et al. 2008; Pastorello et al. 2008; Folatelli et al. 2015), SN 2011dh (a yellow supergiant with $M_{\rm in} \sim$ 12–15 $M_{\odot}$; Maund et al. 2011; Van Dyk et al. 2011, 2013; Ergon et al. 2014), and SN 2013df (see details later). In other cases, analysis of early light curves and/or the interactions with the circumstellar matter (CSM) originating from pre-explosion mass-loss processes offer a chance to constrain the exploding star. Spectral analysis of light echoes showed that Cassiopeia A (hereafter Cas A) was also a Type IIb explosion (Krause et al. 2008). The detailed study of this object can provide valuable pieces of information about the explosion mechanism of SN IIb, which are difficult to extract from studying of the early supernova phases. Such an interesting result was the confirmation of the asymmetric explosion of Cas A (DeLaney et al. 2010; Rest et al. 2011; Fesen & Milisavljevic 2016).

Based on the observational characteristics, SN IIb may be divided into two subgroups (Chevalier & Soderberg 2010). SN 1993J and some similar explosions, e.g. SNe 2011hs (Bufano et al. 2014) and 2013fu (Kumar et al. 2013; Morales-Garoffolo et al. 2015), are thought have arisen from massive stars with extended H envelopes ($R \sim 10^{13}$ cm or some hundreds of solar radii). Other SN IIb seem to have much more compact ($R \sim 10^{11}$ cm, ∼1–2 $R_{\odot}$) progenitors, e.g. SN 2008ax, SN 2003bg or SN 2001ig. Members of these two subgroups are sometimes called SN eIIb (extended IIb) and SN cIIb (compact IIb), respectively. Nevertheless, the classification of SN 2011dh was ambiguous at first. While it was classified as a cIIb based on its early-time luminosity and radio emission (Arcavi et al. 2011), later studies – based on the modelling of the bolometric light curve (Bersten et al. 2012), on comparative multiwavelength studies (Horesh et al. 2013), and on study of late-time X-ray data (Maeda et al. 2014) – strengthen the interpretation as an intermediate case ($R_{\rm in} \sim$ a few tens of $R_{\odot}$) in agreement with the results of the direct progenitor identification (see above). This case illustrates that there are several open questions concerning this subclassification. Moreover, there are other aspects which should be taken into account, e.g. the interpretation of early-time radio data (see e.g. Bufano et al. 2014) or the possible asphericity of the explosions (Mauerhan et al. 2015). None the less, as Ben-Ami et al. (2015) report, the amount of the early-time UV excess can be also a good indicator of the size of the progenitor (although, as the authors also noted, the number of the studied SNe is too low to draw a very general conclusion). The reality is likely to be complicated, because, based on theoretical and observational results, the progenitors of SN IIb explosions may be members of interacting binary systems (see e.g. Woosley et al. 1994; Maund et al. 2004, 2007; Silverman et al. 2009; Claeys et al. 2011; Dessart et al. 2011; Benvenuto, Bersten & Nomoto 2013).

A well-known general characteristic of SN IIb is the presence of double-peaked light curves in the whole optical range, which was first observed in the case of SN 1993J. The rapid decline after the initial peak is interpreted as adiabatic cooling of the 'fireball' after the SN shock has broken out through the star's surface; the timescale of the cooling depends mainly on the radius of the progenitor (see e.g. Chevalier & Fransson 2008; Bersten et al. 2012). As a result of thermalization of γ-rays and positrons originating from the radioactive decay of ^{56}Ni and ^{56}Co, the light curves reach a secondary maximum. The length of the initial declining phase is usually some days, so the fireball phase is not easy to detect (see Section 4.1). Up to now, detailed analyses have been published on only a few SN IIb observed from the very early phases. Thus, it is important to study well-observed individual objects as thoroughly as possible.

SN 2013df is a recently discovered, nearby SN IIb. This object, located 32 arcsec east and 14 arcsec south from the centre of the spiral galaxy NGC 4414, was discovered on 2013 June 8 (Ciabattari et al. 2013). The first spectrum, obtained by Cenko et al. (2013), showed clear resemblance to the early spectra of SN 1993J, which suggested that SN 2013df was an SN IIb. This suspicion was verified by Van Dyk et al. (2014, hereafter VD14), who presented early photometric and spectroscopic data and reached conclusions concerning the properties of the progenitor, identifying it as a yellow supergiant star with an estimated initial mass of $M_{\rm in} \sim$ 13–17 $M_{\odot}$, an effective temperature of $T_{\rm eff} \sim$ 4250 K, and an initial radius of $R_{\rm eff} \sim$ 545 $R_{\odot}$. Morales-Garoffolo et al. (2014, hereafter MG14) presented a detailed analysis of early UV-optical light curves and some spectra, including nebular ones. Their results concerning the progenitor are compatible with those of VD14 ($M_{\rm in} \sim$ 12–13 $M_{\odot}$, $R_{\rm eff} >$ 64–169 $R_{\odot}$). The common main conclusion of these authors is that SN 2013df is very similar to SN 1993J, and it was very probably the endpoint of a massive star with an extended but not massive H envelope. The similarity between SNe 1993J and 2013df was strengthened by the work of Ben-Ami et al. (2015, hereafter BA15) based on the comparison of early UV-optical spectra of several SN IIb. Results based on late-time optical spectroscopy (Maeda et al. 2015), as well as on early and late-time radio and X-ray observations (Kamble et al. 2016), suggest the presence of CSM interactions. This evidence indicates that the extended progenitors, as for SN 2013df, suffer from substantial mass-loss some years before the explosion, which may be caused by the assumed binary companions of the exploding stars.

In this paper, we present some new results concerning the early- and late-time properties of SN 2013df. First, we describe our ground-based spectroscopic and photometric observations in Section 2. The method and results of modelling of spectra using a spectral synthesis code are shown in Section 3. In Section 4, we present the steps of our analysis of the photometric data, including the comparative analysis of early light curves with those of other SN IIb, and the extraction of explosion parameters from early-time bolometric light-curve modelling and from late-time light-curve analysis. At the end of Section 4, we also present our findings concerning the analysis of late-time mid-infrared data of SN 2013df. Finally, in Section 5, we discuss our results and present our conclusions.

2 OBSERVATIONS AND DATA REDUCTION

During the reduction and analysis of our data, we used the adopted values of important parameters of SN 2013df and of its host galaxy, NGC 4414. We adopted the explosion date $t_0 = 2\,456\,447.8 \pm 0.5$ JD, or June 4.3 UT (determined by VD14 from the overall comparison of the SN 2013df light curves with those of SNe 1993J and 2011dh) to calculate the epochs of both spectroscopic and photometric measurements.

Table 1. Adopted values that are used throughout the paper. References: (1) VD14; (2) Freedman et al. (2001).

Parameter	Adopted value	Reference
t_0	2 456 447.8 ± 0.5 JD	1
μ_0	31.10 ± 0.05 mag	2
$E(B-V)_{\rm total}$	0.09 ± 0.01 mag	1

Table 2. Log of spectral observations obtained with HET LRS and IRTF.

UT date	Phase (d)	Instrument	Range (Å)	R (λ/Δλ)
2013-06-13	+9	HET LRS	4172–10 800	300
2013-06-16	+12	HET LRS	4172–10 800	300
2013-06-23	+19	HET LRS	4172–10 800	300
2013-06-27	+23	HET LRS	4172–10 800	300
2013-07-01	+27	HET LRS	4172–10 800	300
2013-07-02	+28	IRTF	6500–25 430	200
2013-07-08	+34	HET LRS	4172–10 800	300

Notes. Phases are given relative to the explosion date (t_0 = 2456 447.8 ± 0.5 JD, or June 4.3 UT) determined by VD14.

We used the distance modulus of the host galaxy $\mu_0 = 31.10 \pm 0.05$ mag ($D = 16.6 \pm 0.4$ Mpc), established by Freedman et al. (2001) based on their study of Cepheid stars. This value was used also by VD14. This distance modulus is definitely lower than the one used by MG14 ($\mu_0 = 31.65 \pm 0.30$ mag), which results in significant differences in the calculated bolometric magnitudes and luminosities of the SN (see Section 4, note that the value used by MG14 cannot be the weighted mean value of distance moduli provided by the NASA/IPAC extragalactic data base, NED,[1] as the authors refer to it; the mean value of individually referenced moduli listed in NED is $\mu_0 = 31.23 \pm 0.54$ mag). The lower value of the distance is also suggested by the published values of the redshift of the host, $z = 0.002\,388$ (given by NED; Rhee & van Albada 1996), and $z = 0.002\,874$ (determined from the position of Na I D lines associated with the host, VD14), which correspond to distances of ∼10.3 and ∼12.4 Mpc, respectively (Wright 2006).

We adopted $E(B-V) = 0.09 \pm 0.01$ mag as the total reddening for SN 2013df from the work of VD14 who determined this value via analysing the Galactic and host-galaxy components of Na I D in their high-resolution spectra.

The adopted values are also shown in Table 1.

2.1 Spectroscopy

We collected a sample of high-quality spectroscopic data on SN 2013df. The object was monitored with the Marcario Low Resolution Spectrograph (LRS) on the 9.2 m Hobby-Eberly Telescope (HET) at McDonald Observatory. Table 2 summarizes the basic details of the 6 spectra ($R = 300$) taken between 2013 June 13 and July 8, during the first month after explosion. All of our HET spectra were reduced using standard techniques (e.g. Silverman et al. 2012). Routine CCD processing and spectrum extraction were completed with IRAF.[2] We obtained the wavelength scale from low-order polynomial fits to calibration-lamp spectra. Small wavelength shifts were then applied to the data after cross-correlating a template sky to the night-sky lines that were extracted with the SN. Using our own IDL routines, we fit spectrophotometric standard-star spectra to the data in order to flux calibrate our spectra and to remove telluric lines (see e.g. Wade & Horne 1988; Matheson et al. 2000). The top panel of Fig. 1 shows the observed HET spectra of SN 2013df, while the comparison of these data with spectra of SNe 1993J and 2011dh is shown in the bottom panel.

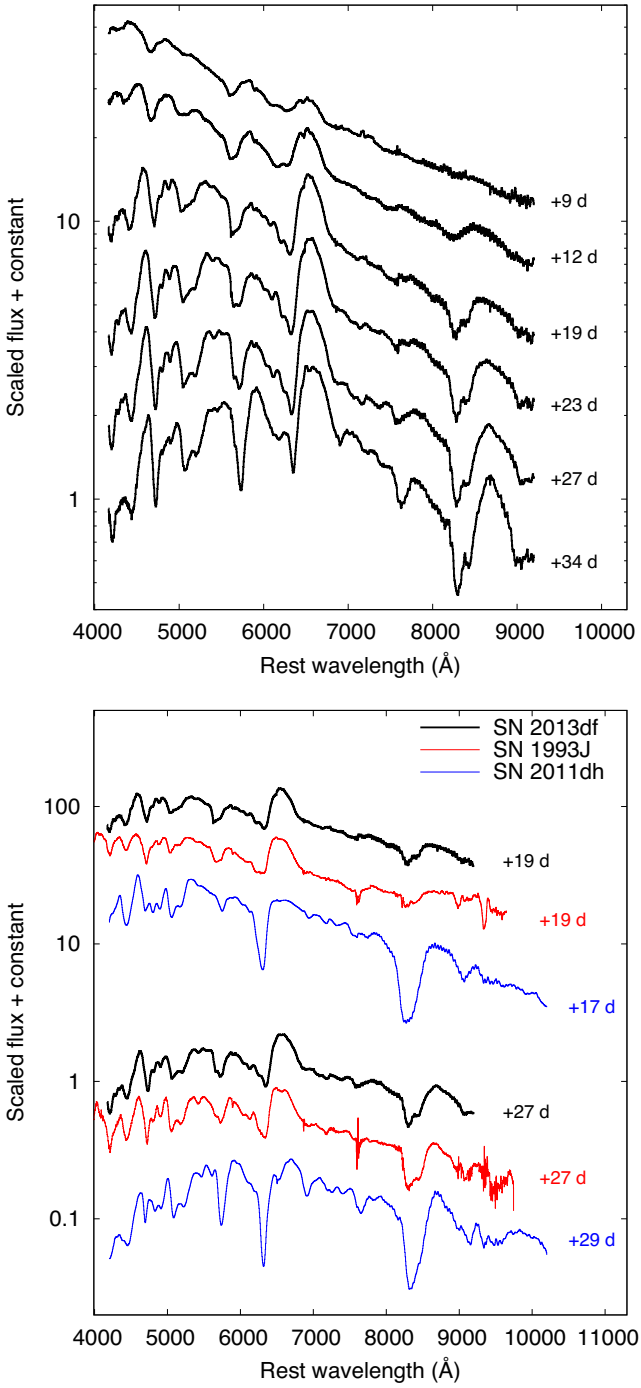

Figure 1. Top: observed HET spectra of SN 2013df. Phases are given relative to the explosion date (t_0 = 2456 447.8 ± 0.5 JD, or June 4.3 UT) determined by VD14. Bottom. Spectra of SN 2013df compared with spectra of other SN IIb 1993J (Barbon et al. 1995) and 2011dh (Marion et al. 2014) at similar ages.

[1] http://ned.ipac.caltech.edu

[2] IRAF is distributed by the National Optical Astronomy Observatories, which are operated by the Association of Universities for Research in Astronomy, Inc., under cooperative agreement with the National Science Foundation.

Additionally, a low-resolution ($R \approx 200$, $\lambda = 0.65$–2.5 μm) near-infrared (NIR) spectrum was also obtained on July 2 (+28 d) with the 3 metre telescope at the NASA Infrared Telescope Facility (IRTF) using the SpeX medium-resolution spectrograph (Rayner et al. 2003). IRTF data are reduced using a package of IDL routines specifically designed for the reduction of SpeX data (Spextool version 3.4; Cushing, Vacca & Rayner 2004).

2.2 Photometry

The photometric observations for SN 2013df were obtained using three different ground-based telescopes. We used the 0.6/0.9 m Schmidt-telescope (Piszkéstető Mountain Station of Konkoly Observatory, Hungary) with the attached 4096 × 4096 CCD (FoV 70 × 70 arcmin^2) equipped with Bessel *BVRI* filters; the 0.5 m Baja Astronomical Robotic Telescope (BART; Baja Observatory, Hungary) with a 4096 × 4096 front illuminated Apogee U16 CCD (FoV 40 × 40 arcmin^2; the frames were taken with 2 × 2 binning) equipped with Sloan $g'r'i'z'$ filters; and the 0.45 m ROTSE-IIIb telescope at McDonald Observatory, operated with an unfiltered CCD with broad wavelength transmission from 3000 to 10 600 Å.

Photometric follow-up observations with the first two telescopes started at +8 d, and continued up to +45 d. To obtain the Konkoly *BVRI* magnitudes, we carried out point spread function photometry on the SN and two local comparison (tertiary standard) stars using the DAOPHOT/ALLSTAR task in IRAF. We applied an aperture radius of 6 arcsec and a background annulus from 7 to 12 arcsec for SN 2013df as well as for the local comparison stars. The instrumental magnitudes were transformed to the standard system applying the following equations:

$$\begin{aligned} V - v &= C_{\rm V}(V - I) + \zeta_{\rm V} \\ (B - V) &= C_{\rm BV}(b - v) + \zeta_{\rm BV} \\ (V - R) &= C_{\rm VR}(v - r) + \zeta_{\rm VR} \\ (V - I) &= C_{\rm VI}(v - i) + \zeta_{\rm VI}, \end{aligned} \quad (1)$$

where lowercase and uppercase letters denote instrumental and standard magnitudes, respectively. The colour terms ($C_{\rm X}$) were determined by measuring Landolt standard stars in the field of PG1633 (Landolt 1992) observed during photometric conditions: $C_{\rm V} = -0.025$, $C_{\rm BV} = 1.268$, $C_{\rm VR} = 1.024$, $C_{\rm VI} = 0.964$. These values were kept fixed while computing the standard magnitudes for the whole data set. Zero-points ($\zeta_{\rm X}$) for each night were measured using the local tertiary standard stars mentioned above. These local comparison stars were tied to the Landolt standards during the photometric calibration.

The $g'r'i'z'$ data from Baja Observatory were standardized using ∼100 stars within the ∼40 × 40 arcmin^2 field of view around the SN, taken from the SDSS DR12 catalogue. In order to avoid selecting saturated stars from the SDSS catalogue, a magnitude cut $14 < r' < 18$ was applied during the photometric calibration.

The SN 2013df position is outside the regular ROTSE-III supernova search fields; however, we scheduled the ROTSE-IIIb telescope for extended follow-up. Up to 30 exposures were taken per night of observation when the weather was supportive. Open CCD data were taken from +11 d to +82 d, and then from +157 d to +237 d. In all cases, data from each day are co-added. The ROTSE data were first calibrated to USNO B1.0 R2-band. A deep template of the host was taken in early 2015 when the SN was well below the detection limit. This template was used to assess the sky-subtracted host flux in the photometric aperture for each epoch, accounting for focus variations during the observing period. Because of the position of the source near the host nucleus, we compared the co-adds of the first and second half of the nightly images to extract a systematic uncertainty per epoch. We also examined the photometry of nearby reference stars and extracted a separate systematic uncertainty from the rms of reference star residuals at each epoch.

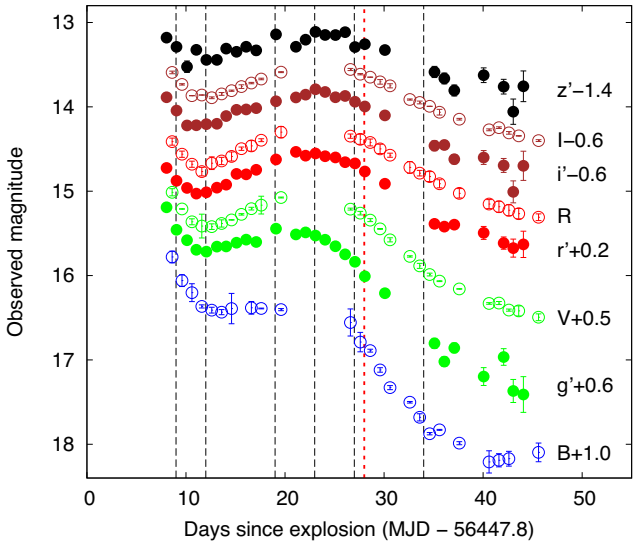

Figure 2. Standard optical light curves of SN 2013df (open circles: *BVRI*, filled circles: $g'r'i'z'$). The vertical dashed lines mark the epochs of spectral observations (dashed lines: HET LRS, red dotted line: IRTF).

During the reduction of ROTSE data, epochs with rms >0.4 mag were rejected from the light curve. All systematic uncertainties are considered to be uncorrelated epoch-to-epoch. The ROTSE data are compared to interpolated Konkoly *R* data from +9 to +40 d, and an offset correction of 0.030 mag is obtained with a $\chi^2/dof = 1.04$. We took the rms value (0.175 mag) of the residuals around this fit as an additional uncorrelated systematic uncertainty on these points. We utilized the *R*-band data for our measurements and derived an offset correction of this data relative to the Konkoly *R*-band data from +7 to +43 d. This yields a 0.05 mag correction to MG14, with a $\chi^2/dof = 1.93$. The data exhibit some deviation from the corresponding Konkoly data early and late in the second peak.

The Konkoly *BVRI*, Baja $g'r'i'z'$, and unfiltered ROTSE-IIIb magnitudes are presented in Tables A1–A3, respectively. Errors (given in parentheses) contain both the uncertainties of the photometry and the standard transformation (or, in the case of ROTSE magnitudes, the uncertainties of calibrations). The standard *BVRI* and $g'r'i'z'$ light curves are shown in Fig. 2, in which we also marked the epochs of our spectral observations. The ROTSE data, as well as the comparison of different light curves and their detailed analysis are presented in Section 4.

The optical data were supplemented by the available data of the *Swift's Ultraviolet/Optical Telescope* (UVOT). We reduced these data using standard HEASOFT tasks: individual frames were summed with the *uvotimsum* task, and magnitudes were determined via aperture photometry using the task *uvotsource*. Since our results agree within the uncertainties with the ones published by MG14, we do not analyse these data in detail. At the same time, we used the *Swift* magnitudes to construct the bolometric light curve (see Section 4.2).

3 SPECTRAL ANALYSIS

While VD14 published only one spectrum obtained at +37 d, MG14 presented a complex study partly based on four photospheric and

Table 3. The photospheric velocities and temperatures of SN 2013df, as found by SYNAPPS.

Date	Epoch	$v_{\rm phot}$ (km s^{-1})	$T_{\rm phot}$ (K)
2013-06-13	+9	14 100	8000
2013-06-16	+12	11 800	7600
2013-06-23	+19	10 800	6800
2013-06-27	+23	8450	6500
2013-07-01	+27	8660	6000
2013-07-08	+34	8000	5800

two nebular spectra. In both papers, the line identification was based on spectral comparison of SN 2013df and other, previously studied SN IIb. BA15 presented four *Hubble Space Telescope* (*HST*) UV-optical spectra obtained in the photospheric phase. They used their own Monte Carlo radiative-transfer code in order to produce synthetic spectra and study the structure of the ejecta of SN 2013df. While they got a good match between the observed and synthetic spectra at wavelengths longer than 5000 Å, their fits are less satisfying at shorter wavelengths (as the authors noted, the reason for the underestimation of the fluxes below 5000 Å might be the interaction of the SN blast wave and circumstellar material).

While the cited papers contain many interesting results concerning SN 2013df, our conclusions based on the thorough analysis of our well-sampled spectral data set obtained over the first month after explosion can deepen this understanding. In this section, we describe the results of our modelling carried out using a spectrum synthesis code, and present our findings concerning the evolution of the main spectral components, especially H I and He I lines.

3.1 Spectral modelling

We applied the parametrized resonance scattering code SYN++ in combination with SYNAPPS[3] (Thomas, Nugent & Meza 2011) to model the spectroscopic evolution of SN 2013df (hereafter we refer only to SYNAPPS). Detailed spectral modelling based on this code – or on SYNOW, the original version of these kind of codes (see e.g. Jeffery & Branch 1990; Branch 2001) – were carried out only in a few cases of SN IIb: 1993J (Elmhamdi et al. 2006), 2010as (Folatelli et al. 2014), 2011dh (Sahu, Anupama & Chakradhari 2013; Marion et al. 2014), 2011ei (Milisavljevic et al. 2013), and 2011fu (Kumar et al. 2013). Since the spectral similarity is very close between SNe 2013df and 1993J (see the bottom panel of Fig. 1), we used Elmhamdi et al. (2006) as a starting point in our modelling, as well as the paper of Mazzali et al. (2009) about SN 2003bg. Before the fitting, all spectra were corrected for the total reddening and the redshift of the host galaxy.

Our SYNAPPS modelling shows a continuously decreasing photospheric temperature from 8000 K (+9 d) to 5800 K (+34 d). This agrees well with the results of both the spectral modelling of BA15 and the blackbody-fitting of the spectral continua carried out by MG14, as well as with the results concerning the modelling of SN 1993J (Elmhamdi et al. 2006). The photospheric velocity drops in our models from 14 to 8000 km s^{-1} during the first month after explosion (see Table 3). These values are significantly larger than those published by BA15 (9600 km s^{-1} at +13 d and 5900 km s^{-1} at +26 d), but are in closer agreement with the results of Elmhamdi et al. (2006) for SN 1993J (9000 km s^{-1} at +16 d and 8000 km s^{-1} at +24 d).

[3] Software was retrieved from https://c3.lbl.gov/es/

Best-fitting SYNAPPS models of two selected spectra (+9 and +27 d), and the contribution of the single elements to the model spectra are shown in Fig. 3. As the bottom panels show, H I, He I, Si II, and Mg II are the most abundant ions in the ejecta in the earliest phase, while the Ca II NIR triplet, the O I λ7774 line, as well as Fe II and Ti II features become strong after +19 d (which is around the epoch of the optical photometric maximum, see Fig. 2). Based on our modelling, the ∼4200–5000 Å region in the post-maximum spectra may be a complex blend of H γ, He I λ4471, Fe II and Ti II lines. This agrees well with the line identifications of BA15, except that they found Co II being dominant instead of Ti II in this region.

Since it is always a key point in the studies of Type IIb/Ib/Ic SNe, we also examined the evolution of H I and He I lines in detail. As can be seen in Figs 1 and 3, there is a broad, two-component absorption profile at ∼6200 Å. This is a common feature in the photospheric spectra of SN IIb (Matheson et al. 2000, 2001) and SN Ib (see e.g. Wheeler et al. 1994; Branch et al. 2002; Folatelli et al. 2006; Hachinger et al. 2012; Reilly et al. 2016, and references therein). While the red component of this absorption feature belongs obviously to the P Cygni profile of the H α line, the origin of the blue component cannot be determined unambiguously. Several authors have suggested that the blue component also belongs to the H α line, e.g. due to the presence of a non-spherical density distribution of H (see e.g. Schmidt et al. 1993; MG14), or of a second, outer layer of H producing high-velocity (HV) H α lines (see e.g. Zhang et al. 1995; Branch et al. 2002; Folatelli et al. 2014; Marion et al. 2014). At the same time, the blending of photospheric H α with other ions, e.g. C II λ6580 or more likely Si II λ6355 (see the latter case e.g. in Mazzali et al. 2009; Silverman et al. 2009; Hachinger et al. 2012) can be also an alternative explanation.

In the case of SN 2013df, we suggest that the presence of Si II is a viable option to explain the source of the blue component of the broad absorption profile at 6200 Å. In our SYNAPPS models, we were able to fit this feature with Si II at each epoch using the temperatures and photospheric velocities mentioned above. We found that the line strength of Si II λ6355 decreased continuously in time, similarly to the cases of SN 2001ig (Silverman et al. 2009) and SN 2003bg (Mazzali et al. 2009). Radiative transfer simulations of SN IIb/Ib/Ic spectra also predict the presence of freshly synthesized Si in the photospheric phase (Dessart et al. 2011; Hachinger et al. 2012); however, Hachinger et al. (2012) note that in more H-rich cases (i.e. SN IIb) the HV wing of H α may dominate over the Si II λ6355 profile. In the case of SN 2013df, we did not find any signs of HV H β lines, which may be an argument against the presence of HV H in the outer layers of the ejecta. At the same time, as Marion et al. (2014) described in their study of SN 2011dh, it is possible that the presence of an outer H region does not produce HV lines except in the case of H α. As a conclusion, we do not rule out that this puzzling feature corresponds to HV H, but we suggest that its source is more probably Si II.

Another factor that makes the identification of the ∼6200 Å profile ambiguous is that there are some difficulties in fitting the P Cygni profile of H Balmer lines in the spectra of SN 2013df with SYNAPPS. On the one hand, H α and H β absorption lines cannot be fitted contemporaneously with a given set of parameters of H lines (in Fig. 3, we present the solution where H β line is well fitted). On the other hand, there is also a general inconsistency in the fitting of the absorption and emission components of the H α line. The same problem was described by Elmhamdi et al. (2006) and Kumar et al. (2013) concerning the SYNOW modelling of the spectra of SNe 1993J and 2011fu, respectively, and can be also seen in the results of Sahu et al. (2013) concerning SYN++ modelling of some pre-maximum

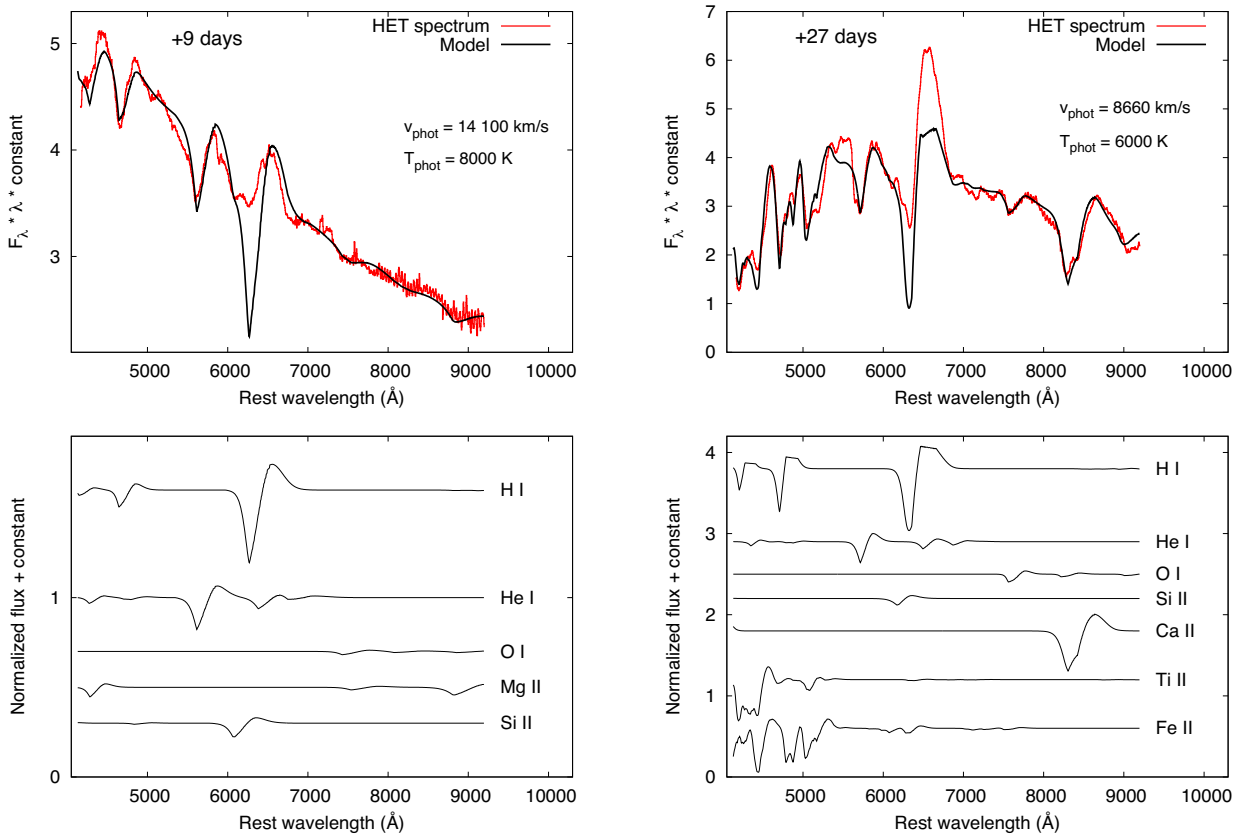

Figure 3. Best-fitting SYNAPPS models of two selected spectra (+9 and +27 d), and the contribution of the single elements to the model spectra.

spectra of SN 2011dh. This modelling problem may be caused by a still unrevealed blending effect, or, more probably, by the fact that one of the basic assumptions of SYNOW and SYNAPPS codes is local thermodynamic equilibrium (LTE) for level populations. While the presence of non-LTE effects seems to be a plausible explanation for the differences of the observed and synthetic spectra, we note that BA15 were also unable to fit the P Cygni profile of H α adequately, although they used a radiative-transfer code that includes abundance stratification and a module that calculates the ionization of H and He in full non-LTE (see references in BA15).

To get the best-fitting models of the post-maximum spectra, the H lines need to be detached from the photosphere by $\sim$1000 km s^{-1}. This results flat-topped H emission components in the model of the +27 d spectrum; however, we were not able to check whether this effect can be real or not. The emission components of H α and H β are blended with the He I λ6678 line and metal lines, respectively, and the inconsistencies concerning the contemporaneous fit of H α and H β lines makes this examination even more difficult. Nevertheless, we note that 1000 km s^{-1} is at the limit of uncertainty in SYNAPPS fits, so this may not be a real separation.

The other interesting topic is the evolution of He lines. As can be seen in Figs 1 and 3, as well as in other SN IIb, He I λ5876 is already identifiable in the pre-maximum spectra, and its intensity is continuously growing. While this feature is often referred as to a blend of He I and Na I D, our modelling shows that the contribution of Na I to this feature is negligible (see the details later).

We also identified other He I lines in the spectra of SN 2013df. In our HET spectra, the λ6678 and λ7065 lines are identifiable as early as +9 d and +19 d, respectively, in contrast to the results of MG14 who stated that these lines are not visible before +40 d (using June 4.3 UT as the explosion date). The λ5016 line becomes visible at +19 d. The He I λ4471 line, although it is the strongest He line after λ5876, is not obviously identifiable in our HET spectra. On the one hand, the blue end of the observed spectral region is at 4170 Å, very close to the blue wing of the suggested He I line. On the other hand, the observed feature at $\sim$4200–4300 Å may be a complex blend of He I, H γ and Mg II, or, of He I, H γ, Ti II and Fe II (before and after maximum, respectively).

We also note that we did not find convincing evidence for non-thermal excitation of the He features during the early phases of SN 2013df sampled by our spectra, contrary to the findings of Ergon et al. (2014) in SN 2011dh. Such an effect is usually invoked to explain the increase of the optical depth of the He I features as a function of phase, contrary to the expectations from the Sobolev approximation.

3.2 'HV' helium in the ejecta

During the analysis of the evolution of He I lines, we discerned that the absorption profile at $\sim$5650 Å, which we first identified as the He I λ5876 line, actually consists of two components. As Fig. 4 shows, there seems to be a single absorption line with a continuously decreasing velocity in the pre-maximum phases (up to +19 d); however, as the spectra evolves, it develops a double-troughed feature. The red component becomes dominant by +34 d.

While the origin and evolution of the double-troughed 6200 Å profile are discussed in several papers on SN IIb, the similar structure of the 5650 Å profile does not seem to be a common phenomenon. Up to now, the only discussion of the double-troughed structure of the He I λ5876 line was for SN 1993J (Schmidt et al.

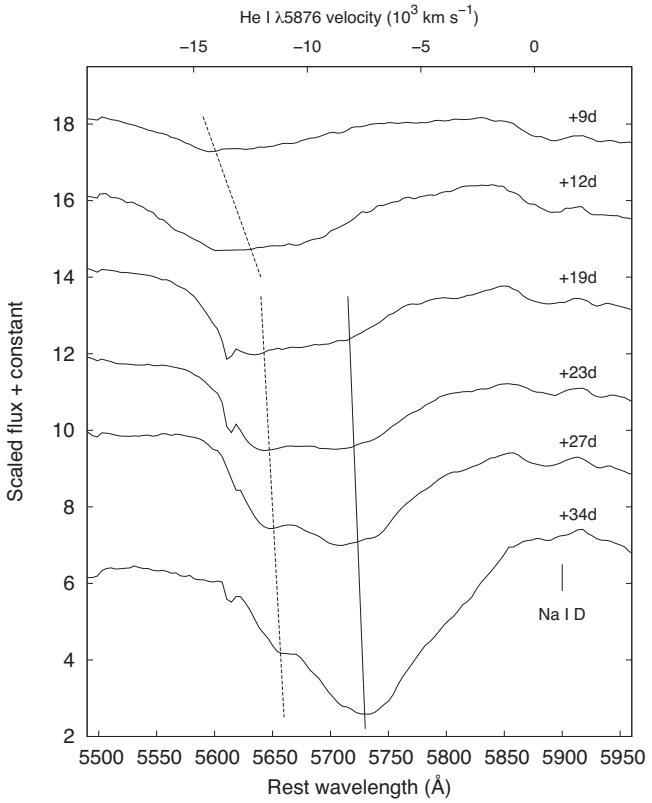

Figure 4. Evolution of the He I λ5876 line in the spectra of SN 2013df. Solid and dashed vertical lines mark the positions of 'low'- and 'high-velocity' He I features, respectively. The weak feature at ∼5900 Å is the unresolved sum of interstellar Na I D lines originating from the Milky Way and the host.

1993; Zhang et al. 1995). Based on the explanation of Schmidt et al. (1993), the shape of this feature, as well as the similar double-troughed profile of the H α line, may be a sign of asymmetry in the expanding material. The presence of this asymmetry is also supported by the results of spectropolarimetric studies of SN 1993J (Trammell, Hines & Wheeler 1993; Höflich 1995; Höflich et al. 1996; Tran et al. 1997); similar findings have been published later based on spectropolarimetry of several other SN IIb (see Mauerhan et al. 2015, and references therein), as well as the on the high-resolution imaging of Cas A and the spectral studies of its light echoes (see e.g. DeLaney et al. 2010; Rest et al. 2011).

Zhang et al. (1995) also studied the spectroscopic evolution of the broad H α and He I λ5876 absorption features. Instead of assuming an asymmetric explosion, they suggested a model with a two-component density structure of the ejecta (a shallower layer immediately outside a steeply decreasing inner envelope) to explain the shape of H and He features. Using this two-component model, they were able to reproduce the H and He line profiles better than in the cases when they used models based on a single power-law density structure.

The top-left panel of Fig. 5 shows the series of spectra of SN 1993J (published by Barbon et al. 1995) in the region of 5500–5950 Å from +10 to +26 d after explosion. The double-troughed structure of the 5650 Å profile is clearly seen, and is very similar to that of SN 2013df.

Another SN IIb that seems to show a double-troughed 5650 Å profile is SN 2011fu. Kumar et al. (2013) did not study this profile in detail; however, it is not so easy to see the phenomenon in their spectra because of the low signal-to-noise ratio of the data and the lack of observations between +14 and +27 d after explosion. We present here the earliest five spectra from their paper in the top-right panel of Fig. 5; the 5650 Å profile clearly has a double-troughed shape at +27 d (the data were smoothed here by a 20 Å-wide window function for better visibility). Morales-Garoffolo et al. (2015) presented high-quality spectra of SN 2011fu including data taken at +17, +20 and +27 d. While they noted that around a month past explosion the He I λ5876 absorption component had a complex profile with a double trough, they did not analyse the profile in detail.

We also checked all the available spectra of other SN IIb. We did not see this double minimum either in our data of SN 2011dh (published in Marion et al. 2014) or in any other cases where the first 30–40 d are well sampled:[4] SNe 1996cb, 1998fa (both from Modjaz et al. 2014), 2000H (Branch et al. 2002; Modjaz et al. 2014), 2001ig (Silverman et al. 2009), 2003bg (Hamuy et al. 2009), 2005U, 2006T, 2006el, 2008aq (all from Modjaz et al. 2014), 2008ax (Taubenberger et al. 2011; Modjaz et al. 2014), 2008bo, 2008cw (both from Modjaz et al. 2014), 2011hs (Bufano et al. 2014), and 2013bb (unpublished PESSTO[5] data). We found three other SN IIb with well-sampled spectroscopic data sets: SNe 2009mg (Oates et al. 2012), 2010as (Folatelli et al. 2014), and 2011ei (Milisavljevic et al. 2013). These data are not publicly available; however, the published data seem to show the double-troughed 5650 Å profile in none of these cases. We present the early spectral evolution of two of the listed SNe, 2008ax and 2011dh, in the bottom panels of Fig. 5.

While Schmidt et al. (1993) and Zhang et al. (1995) suggested that the double-troughed appearance of the ∼5650 Å feature may be caused by the asymmetry of the explosion or the spatial distribution of He in the ejecta, respectively, we also examined other possibilities. This feature is generally interpreted as the unresolved blend of He I λ5876 and Na I D lines. Nevertheless, we think that Na I D probably does not interfere here. Looking at Fig. 4, we can see that the velocity of the ∼5650 Å feature is ∼14 000 km s^{-1} with respect to the rest wavelength of He I λ5876 at the first epoch. Na I D has higher rest wavelength, so if the feature at ∼5650 Å is Na I instead of He I, it should have even higher velocity than 14 000 km s^{-1} (which value matches pretty well with the velocity of H α and with the global photospheric velocity determined by SYNAPPS, see Fig. 6 and Table 3, respectively). Later, when the lower velocity components take over, the assumption that it is Na I instead of He I would, again, imply that Na I is at ∼8500–9000 km s^{-1}, which is still a higher value than those of the rest of the photospheric features.

Our SYNAPPS models also suggest that the contribution of local Na I to the spectra of SN 2013df is negligible (we note that this is also in agreement with the modelling results of BA15). Since our models adequately fit the spectra, and we did not find any other elements that have lines around 5650 Å (see Fig. 3), we assume, as do Schmidt et al. (1993) and Zhang et al. (1995), that both absorption features belong to the He I λ5876 line. To verify this statement, we also examined the evolution of other He lines in the spectra of SN 2013df. As we mentioned above, the other He lines in the observed spectral range are all weak and/or blended; however, if we take a closer look at He I λ6678 at the top of the emission of the H α line, we can see a weak double-troughed profile evolving similarly as λ5876 (see Fig. 7).

[4] We downloaded these data from WISeREP (Weizmann Interactive Supernova data REPository), http://www.weizmann.ac.il/astrophysics/wiserep, Yaron & Gal-Yam (2012).

[5] Public ESO Spectroscopic Survey of Transient Objects, www.pessto.org

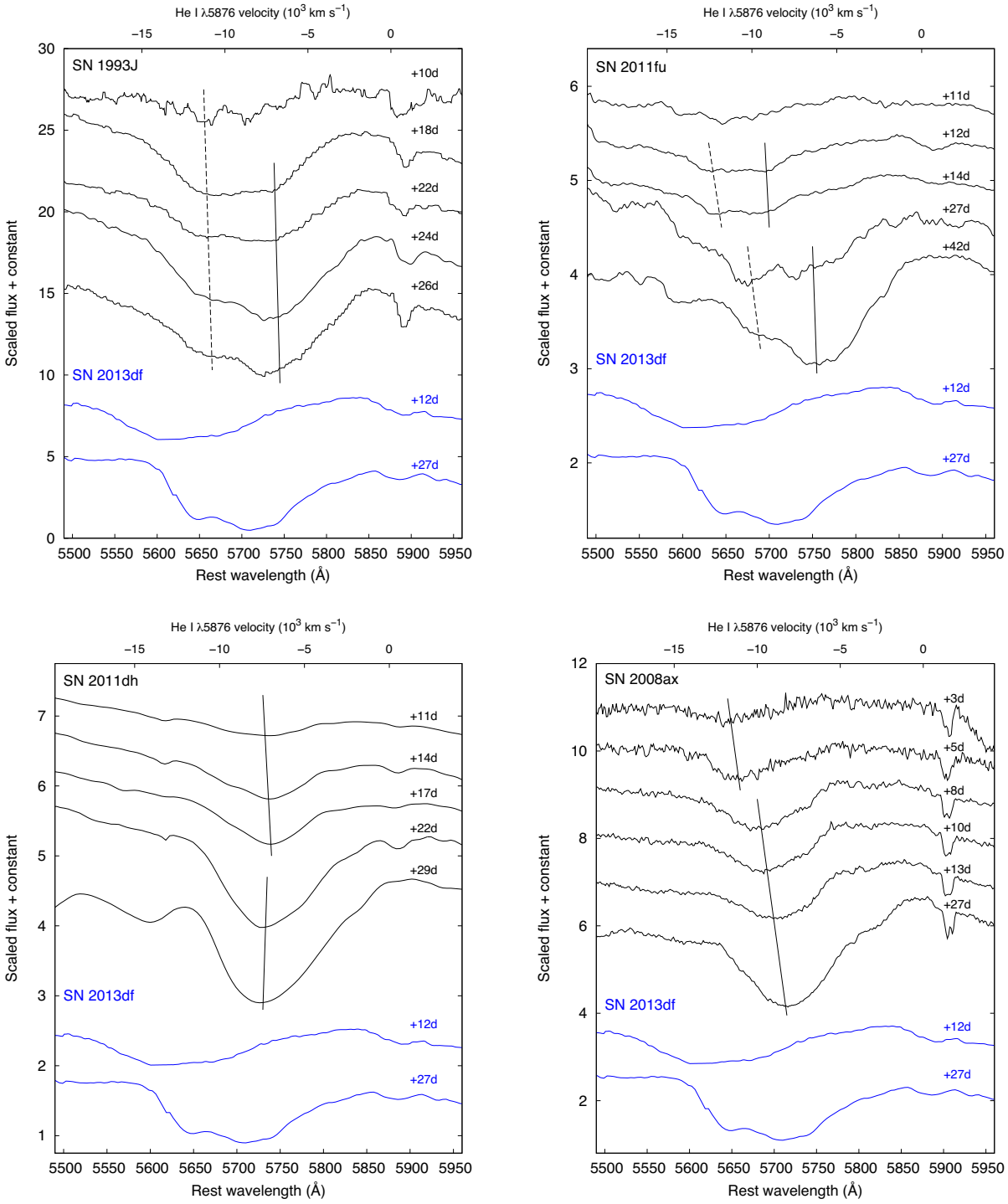

Figure 5. Spectral evolution of four different SN IIb between 5500 and 5950 Å: SN 1993J (Barbon et al. 1995, top left), SN 2011fu (Kumar et al. 2013, top right), SN 2011dh (Marion et al. 2014, bottom left), and SN 2008ax (Taubenberger et al. 2011; Modjaz et al. 2014, bottom right). The spectra of SNe 1993J and 2011fu show a double-troughed He I λ5876 profile similarly to SN 2013df, while there are no obvious similar effects in the other two cases shown in the bottom panels. Solid and dashed vertical lines mark the positions of 'low'- and 'high-velocity' He I features, respectively. The +12 d and +27 d spectra of SN 2013df are also shown on each panel for a comparison. All spectra were corrected to the redshifts of the host galaxies. The spectra of SN 2011fu were smoothed by a 20 Å-wide window function for better visibility. All the redshift and age information was adopted from the original papers.

An independent check on the behaviour of the He lines would be to examine He I lines in the NIR spectral range (λλ 10830, 20581). Unfortunately, we have only a post-maximum NIR spectrum, thus, we were not able to follow the evolution of these He I lines during the photospheric phase, as well as to check whether they also show double-troughed profiles in the early phases or not. Our single NIR spectrum was obtained nearly contemporaneously with the +27 d optical spectrum (we show the combined optical/NIR spectrum in Fig. 8). As can be seen, the NIR He I lines are found at $v \sim 8000$ km s^{-1}, which agrees well with the velocities of the optical

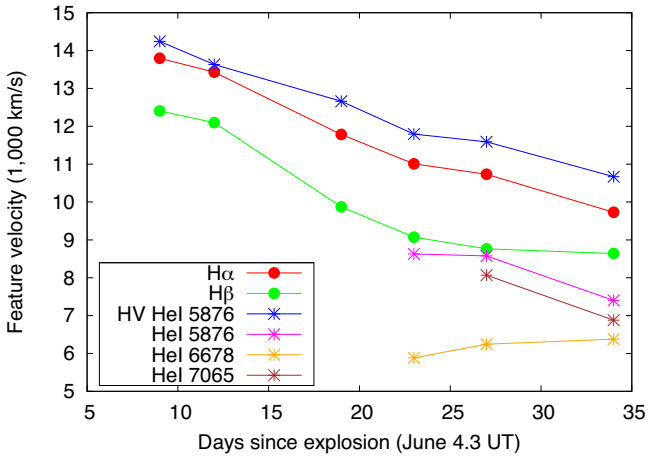

Figure 6. Velocities of some selected lines in the photospheric phase of SN 2013df. Note that the velocity of the He I λ6678 line has a large uncertainty at each epoch; that may explain why its velocity evolution is so different from those of other He lines.

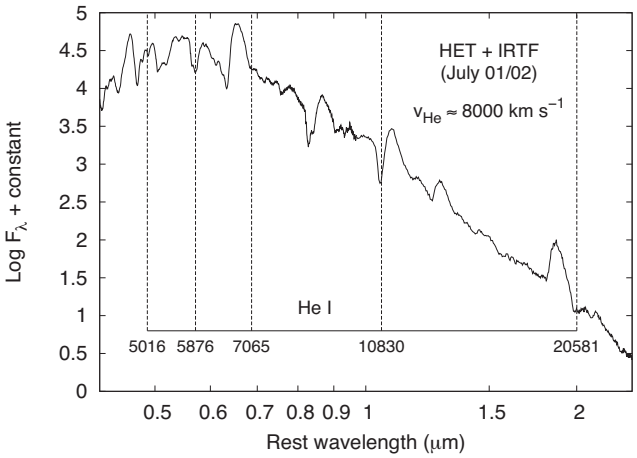

Figure 8. The combined optical/NIR spectrum of SN 2013df at +27/28 d after explosion. The positions of the most significant He I lines (all at $v \sim 8000$ km s^{-1}) are marked with dashed lines.

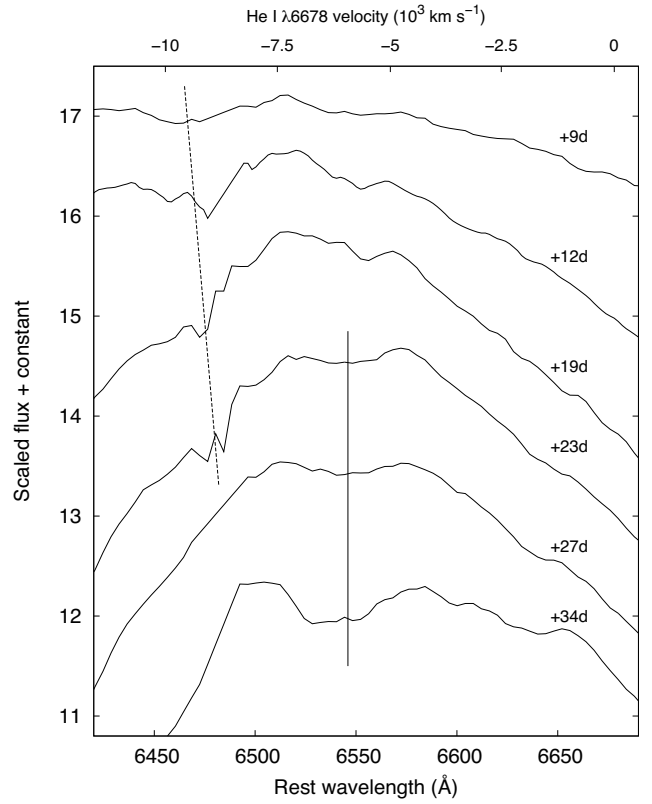

Figure 7. Spectral evolution of the He I λ6678 line in the case of SN 2013df. Solid and dashed vertical lines mark the positions of 'low'- and 'high'-velocity He I features, respectively.

He I lines at this epoch (see Fig. 6). Note that the velocity of the He I λ6678 line has a large uncertainty at each epoch; that may explain why its velocity evolution is so different from those of other He lines.

As discussed e.g. in Marion et al. (2014), the hydrogen velocities usually significantly exceed the helium velocities in the case of either SN Ib (Branch et al. 2002) or SN IIb (see also Chornock et al. 2011; Milisavljevic et al. 2013); the degree of separation can be as large as 4–5000 km s^{-1}. The presence of this separation also agrees with the results of the theoretical work by Dessart et al. (2011). The clear separation of H and He lines in velocity space indicates that the lines of the two elements are formed in separate regions.

Assuming that we see the evolution of He I at ∼5650 Å, Fig. 6 allows us to draw an interesting conclusion. As can be seen in the case of SN 2013df, the 'HV' He I λ5876 component has a similar (actually even a bit higher) velocity to that of the H α line. Instead of the model described above, this effect indicates that both H and He features form in the outermost envelope during the early phases. The evolution of the He I λ5876 line is consistent with the nature of a two-component atmosphere, which consists of an outer H-rich shell mixed with some He and a denser He-rich core. The transition in the line profiles occurs when the photosphere moves back from the shell to the inner core. The mixing of H and He in the outer shell is in agreement with the modelling results of BA15. MG14 found the H and He velocities to be separated by ∼1000–1500 km s^{-1}; however, they do not mention the presence of 'HV' He in the spectra. We note that the velocity of the 'HV' He I λ5876 component is among the highest He line velocities that have ever been observed in SNe IIb. It is comparable to those of SNe Ib (see e.g. fig. 3 of Liu et al. 2015), which tend to show higher He line velocities.

We expected to find similar results concerning both SNe 1993J and 2011fu. In the case of SN 1993J, the results of Barbon et al. (1995) show a quite large separation (∼4000 km s^{-1}) between the H α and He I λ5876 lines. At the same time, if we take into account the presence of the 'HV' He component ($v \sim$ 11–12 000 km s^{-1}), the degree of separation is less than 2000 km s^{-1} (as was previously indicated by the results of Wheeler et al. 1993, and, more recently, by BA15). In the case of SN 2011fu, Morales-Garoffolo et al. (2015) examined the velocity evolution of H α and He I λ5876 lines in detail. Although they found the He I λ5876 line to have a complex profile, they obtained the line velocities by adjusting a single Gaussian to the whole profile. Nevertheless, they found that H α is not clearly separated from He in velocity space, which is in agreement with our findings concerning SNe 2013df and 1993J.

The results of Rest et al. (2011), based on the analysis of light echo spectra of Cas A, are also worth mentioning here. They found the H and He velocities being coincident, for which they gave several possible explanations: a relatively strong mixing of H and He layers, the role of the distribution of ^{56}Ni in the ionization structure of the

outer layers, or the extreme thinness of the outer H layer. Although there is no clear evidence as to whether this SN was a cIIb or an eIIb, the second option (assuming a red supergiant as progenitor) seems to be more probable. The explosion of a compact star can be a viable explanation only in binary progenitor models, but there is no evidence for a companion star to date; however, the merging of two stars into a single one before the explosion may solve this problem (Young et al. 2006; Krause et al. 2008; Claeys et al. 2011). If we suppose the scenario of a single extended progenitor for Cas A, the findings of Rest et al. (2011) fits well into the results described above. While they did not rank the possible explanations of the coinciding H and He velocities, we think that the extreme thinness of the outer H layer is less possible; in this case, we should see this effect also in SNe cIIb.

As a conclusion, it can be pointed out that the evolution of the He I λ5876 profile in the spectra of SN 2013df, as well as the lack of considerable separation of H and He velocities indicates that He lines partially form in the outer regions of the expanding ejecta. Similar spectral properties can be seen in SNe 1993J and 2011fu, as well as in the light echo spectra of Cas A. All of these SNe probably belong to SN eIIb that are thought to have very extended progenitors. On the other hand, as we found, many other SN IIb, which are thought to emerge from more compact progenitors, do not show the presence of 'HV' He lines. The presence of this effect may depend on the degree of the mixing of H and He layers, which may be more significant in red/yellow supergiants than in more compact Wolf–Rayet stars; however, there are several circumstances that may affect the degree of mixing (convection, rotation, presence of a companion etc., see Langer 2012, for a review). All of these factors should be taken into account in a detailed examination of the problem, which is beyond the scope of our paper. For the more detailed studies, it would be also necessary to obtain and analyse high-quality and well-sampled spectral data of other SNe eIIb and cIIb.

4 LIGHT-CURVE ANALYSIS

4.1 Properties of the early-time light curves

MG14 carried out a detailed UV-optical photometric study of SN 2013df, including the analysis of light-curve shapes, colour curves, and the bolometric light curve. Since our data agree well with the observed brightness of the SN published by MG14 (see Fig. 9 showing our *BVRI* data comparing with the results of MG14 and with *Swift* data), we have not repeated every step of the analysis of MG14. Instead, in this section we present some additional results that complement the formerly published ones, or, in some cases, may lead to different conclusions.

SN 2013df is only the third SN IIb, after SNe 1993J (Richmond et al. 1994) and 2011fu (Kumar et al. 2013; Morales-Garoffolo et al. 2015), where the initial declining phase is clearly visible in all optical bandpasses. This effect may be related to the cooling of the extended progenitor envelope after shock-breakout. Similar light-curve evolution seems to be detected in the Sloan g' bandpass in the case of SN 2011dh within some days after explosion (Arcavi et al. 2011; Bersten et al. 2012). Other SN IIb caught in very early phases do not show this effect (see e.g. SN 2013cu; Gal-Yam et al. 2014), or only in the UV and blue bandpasses (see the case of SN 2008ax; Pastorello et al. 2008; Roming et al. 2009). As discussed in Section 1, the detectability of the initial declining phase is thought to be connected with the radius of the progenitor star.

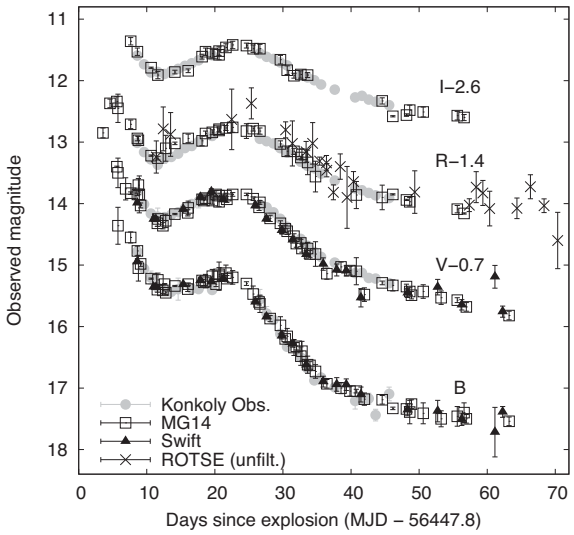

Figure 9. Our *BVRI* measurements of SN 2013df comparing with the results of MG14 and with *Swift* data. Our early-time unfiltered ROTSE measurements are also shown.

SN IIb also show significant inhomogeneity in their secondary peak magnitudes and in the corresponding peak times. We present these parameters for SN 2013df in Table 4, and compare them with those of three other SNe IIb (1993J, 2008ax, and 2011dh) in Table 5. For SNe 2008ax and 2011dh, we adopted the results of Taubenberger et al. (2011) and Sahu et al. (2013), respectively. We re-calculated the peak absolute magnitudes of SN 1993J published by Richmond et al. (1994), because the value of the interstellar reddening in the direction of SN 1993J was very uncertain at the date of publishing (our adopted values of reddening, the distance moduli, and the estimated dates of explosions, together with the corresponding references, are presented in the footnotes of Table 5).

Our results show that SN 2013df was less luminous than SN 1993J. On the other hand, SN 2013df seems to be the spectroscopic 'twin' of SN 1993J, as mentioned above. SN 2013df also seems to be fainter than both SNe 2008ax and 2011dh. There are other faint SN IIb in the literature e.g. SN 1996cb, $M_V \sim -16.2$ mag (Qui et al. 1999), or SN 2011ei, $M_V \sim -16.0$ mag (Milisavljevic et al. 2013). The brightest known SN IIb, SN 2011fu, has a peak magnitude of $M_V \sim -18.5$ mag (Kumar et al. 2013). We thus see that peak magnitudes scatter within a range of more than 2 mag. Looking at the values of secondary peak times (the time elapsed from the moment of explosion), the secondary maximum of SN 2013df occurred at a later epoch in all bands, relative to that of the other three SNe. These findings agree well with the results published by VD14.

We note that the results of MG14 suggest a different conclusion. Adopting a significantly larger value for the distance of the host galaxy (see Section 2), they concluded that SN 2013df was only slightly fainter than SN 1993J ($M_R = -17.71 \pm 0.31$ mag versus -17.88 ± 0.38 mag), so it was brighter than both SNe 2008ax and 2011dh. Contrary to MG14, we accept $\mu_0 = 31.10 \pm 0.05$ mag for the distance modulus of the host of SN 2013df, as determined by Freedman et al. (2001). This value is close to the mean value of the distance moduli in NED ($\mu_0 = 31.23$ mag), and it originates from the same study as the distance modulus of M81 (host of SN 1993J) adopted by us as well as by MG14 (see Table 5).

Table 4. *BVRI* and $g'r'i'z'$ secondary maxima with the corresponding times.

Filter	$t^a_{\rm rise}$ (d)	Apparent max. magnitude (mag)	A_λ (mag)	Absolute max. magnitude (mag)
B	20.39(0.80)	15.31(0.06)	0.42(0.05)	−16.21(0.12)
g'	20.25(0.22)	14.86(0.01)	0.37(0.05)	−16.61(0.08)
V	21.68(0.20)	14.55(0.01)	0.30(0.05)	−16.85(0.08)
R	22.77(0.20)	14.26(0.01)	0.26(0.05)	−17.10(0.08)
r'	22.38(0.12)	14.36(0.01)	0.27(0.05)	−17.01(0.08)
i'	22.78(0.27)	14.44(0.01)	0.20(0.05)	−16.86(0.08)
I	23.29(0.20)	14.12(0.01)	0.19(0.05)	−17.17(0.08)
z'	23.02(0.96)	14.56(0.03)	0.14(0.05)	−16.68(0.09)

Notes. [a]With respect to $t_0 = 2456\,447.8 \pm 0.5$ JD.

Table 5. Comparison of *UBVRI* secondary maximum absolute magnitudes and peak times of four SN IIb.

	SN 1993J[a]		SN 2008ax[b]		SN 2011dh[c]		SN 2013df[d]	
Filter	Peak abs. mag.	$t_{\rm rise}$ (d)	Peak abs. mag.	$t_{\rm rise}$ (d)	Peak abs. mag.	$t_{\rm rise}$ (d)	Peak abs. mag.	$t_{\rm rise}$ (d)
U	-17.40 ± 0.14	19.0	-17.73 ± 0.56	16.7 ± 0.5	-16.19 ± 0.18	15.8 ± 0.5	–	–
B	-17.23 ± 0.13	19.7	-17.32 ± 0.50	18.3 ± 0.5	-16.38 ± 0.18	19.6 ± 0.5	-16.21 ± 0.12	20.39 ± 0.80
V	-17.59 ± 0.13	21.0	-17.61 ± 0.43	20.1 ± 0.4	-17.12 ± 0.18	20.6 ± 0.5	-16.85 ± 0.08	21.68 ± 0.20
R	-17.75 ± 0.12	21.3	-17.69 ± 0.39	21.5 ± 0.4	-17.43 ± 0.18	21.3 ± 0.5	-17.10 ± 0.08	22.77 ± 0.20
I	-17.68 ± 0.12	22.0	-17.75 ± 0.35	22.4 ± 0.7	-17.48 ± 0.18	22.9 ± 0.5	-17.17 ± 0.08	23.29 ± 0.20

Notes. [a]Calculated from the data of Richmond et al. (1994); adopted parameters: $t_0 = 2449\,074.0$, $E(B-V) = 0.19 \pm 0.09$ mag, $\mu_0 = 27.80 \pm 0.08$ mag (Lewis et al. 1994; Freedman et al. 2001; Richardson, Branch & Baron 2006).
[b]Adopted from Taubenberger et al. (2011) using $t_0 = 2454\,528.8 \pm 0.2$, $E(B-V) = 0.40 \pm 0.10$ mag, and $\mu_0 = 29.92 \pm 0.29$ mag.
[c]Adopted from Sahu et al. (2013) using $t_0 = 2455\,712.5 \pm 1.0$, $E(B-V) = 0.035$ mag, and $\mu_0 = 29.62 \pm 0.05$ mag (Vinkó et al. 2012).
[d]Calculated in this work, adopted parameters: $t_0 = 2456\,447.8 \pm 0.5$, $E(B-V) = 0.09 \pm 0.01$ mag, $\mu_0 = 31.10 \pm 0.05$ mag (Freedman et al. 2001; VD14).

There is also a noticeable difference between the secondary peak times of SN 2013df and the ones determined by MG14. This is caused by the difference between the estimated explosion dates (MG14 used $t_0 = 2456\,450.0 \pm 0.9$ JD instead of $2456\,447.8 \pm 0.5$ JD). If we correct their results using our t_0 value, we get all peak times within 0.5 d in the optical (*BVRI*) bands.

4.2 Analysis of the early bolometric light curve

In stripped envelope SNe, it has been observed that the shape of their light curves around the secondary peak looks more-or-less similar (see e.g. Wheeler, Johnson & Clocchiatti 2015, hereafter WJC15). By the analysis of Arnett (1982), this portion of the light curves can be utilized to extract important physical parameters, such as the mass and the initial radius of the ejecta, the initial nickel mass, or the initial thermal and kinetic energy. Several authors have employed this method to study stripped envelope SNe (see e.g. Clocchiatti & Wheeler 1997; Valenti et al. 2008; Cano 2013; Wheeler et al. 2015).

To estimate the values of the main explosion parameters for SN 2013df, we fitted a simple semi-analytic model to the bolometric light curve calculated from our early optical photometric measurements and from the UV data of *Swift*. We constructed this quasi-bolometric light curve using the method described in Marion et al. (2014). To calculate the spectral energy distributions (SEDs) of SN 2013df, we converted the *BVRI* magnitudes to F_λ fluxes using the calibration of Bessell, Castelli & Plez (1998). Since our *BVRI* measurements are not well sampled around the secondary maximum, we calculated the missing values by interpolation using our $g'r'i'z'$ photometry. For the *Swift/UVOT* data, we applied the latest zero-points and flux calibration by Breeveld et al. (2011). The fluxes were dereddened using the Galactic reddening law parametrized by Fitzpatrick & Massa (2007) assuming $R_{\rm V} = 3.1$ and adopting $E(B-V) = 0.09$ mag (see Section 2). The quasi-bolometric light curve was derived by integrating the dereddened F_λ values of the combined UV-optical SEDs over wavelength. The missing far-UV fluxes were estimated by assuming a linearly declining SED below 1928 Å (the central wavelength of *Swift* UW2 filter) reaching zero flux at 1000 Å. The long-wavelength (near-and mid-infrared) contribution was estimated by fitting a Rayleigh–Jeans tail to the red end of the observed SEDs, and integrating it to infinity. Finally, the integrated fluxes were converted to luminosities using $D = 16.6$ Mpc (see Section 2). The luminosity at the secondary maximum is around $L_{\rm bol} \sim 1.1 \times 10^{42}$ erg s^{-1}. We note that this value is approximately a factor of 2 lower than the one published by MG14; this difference may be due to mainly the different values of distance moduli discussed above.

The model we used incorporates recombination and was originally presented by Arnett & Fu (1989); it has been recently extended by Nagy et al. (2014) and Nagy & Vinkó (2016), focusing on SNe II-P and IIb. This extended model assumes a homologously expanding spherical ejecta, and pure Thomson scattering with opacities being constant in a given ionized layer. The model solves the photon diffusion equation in the ejecta, taking into account the energy release of the recombination processes, the radioactive heating of ^{56}Ni and ^{56}Co and the effect of γ-ray leakage (Chatzopoulos, Wheeler & Vinkó 2012).

Double-peaked light curves, as that of SN 2013df, are generally modelled by a two-component ejecta configuration (see e.g. Bersten et al. 2012; Kumar et al. 2013; Nagy & Vinkó 2016). This two-component model contains an extended, low-mass, H-rich outer envelope and a more massive, denser, He-rich inner core. The contribution of the two different components is well separated in time,

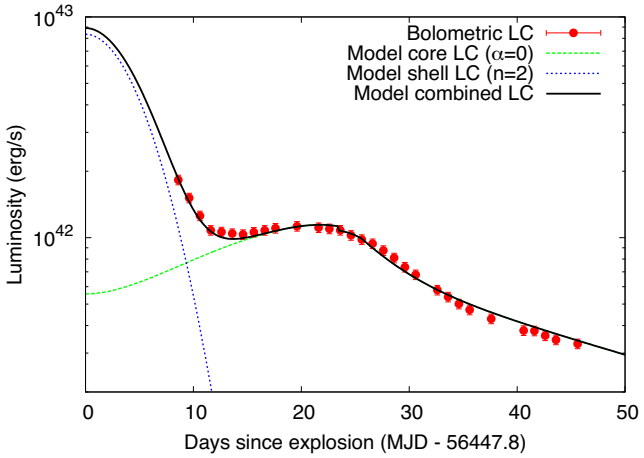

Figure 10. Quasi-bolometric light curve of SN 2013df with the best-fitting semi-analytic model. See the details in the text.

because the photon diffusion time-scale is much lower in the outer region than in the core (see Kumar et al. 2013). At early phases, the radiation from the adiabatically cooling layer of the shock-heated outer envelope dominates the LC, while the second peak is powered by the radioactive decay of ^{56}Ni and ^{56}Co heating the inner core. The shape of the observed light curve can be modelled as the sum of these two processes. We present the quasi-bolometric light curve of SN 2013df with the best-fitting semi-analytic model in Fig. 10.

We used a constant density profile ($\alpha = 0$ within the model of Nagy et al. 2014) for the inner region, while the outer H-rich shell had a power-law density distribution. The best fitting was obtained by using a density profile exponent of $n = 2.0 \pm 0.2$ (α and n were fitted independently). In the outer shell, the energy input from recombination is not significant because of the low mass and the adiabatic expansion of this region.

Choosing proper values for the optical opacities in the inner core as well as in the outer shell is a fundamentally important step in modelling the light curve with a semi-analytic model (see Nagy & Vinkó 2016, for a recent discussion of this issue). Based on our calculations, detailed below, we selected $\kappa \sim 0.4$ and $\sim$0.2 cm^2 g^{-1} for the outer H-rich envelope and the inner He-rich core, respectively. Setting $\kappa \sim 0.3$ cm^2 g^{-1} for the outer envelope (which is closer to the expected mean opacity of a solar-like composition), the best-fitting light curves are practically identical to those from the higher opacity models, resulting in very similar ejecta parameters from the fits.

To verify the reality of the chosen (constant) κ values, we followed the method described in Morozova et al. (2015). We generated a pre-supernova model using MESA[6] (Modules for Experiments in Stellar Astrophysics; Paxton et al. 2011, 2013) 1D stellar evolution code. First, we constructed a single star with an initial mass of $M_{\rm in} = 18.5$ M$_\odot$. Secondly, we removed the large part of the outer H-layer, getting a 7.5 M$_\odot$ star with a 1 M$_\odot$ H-layer as a synthetic SN IIb pre-explosion model. This model was exported to the SNEC[7] (The SuperNova Explosion Code; Morozova et al. 2015) radiation-hydrodynamics code, which computes synthetic bolometric light curves following the expansion of an input pre-supernova model star. We found that the average opacities of those SNEC models that generate double-peaked Type IIb-like light curves are in good agreement with the ones we used during the analytic light-curve modelling of SN 2013df. More details on the comparison between the opacities of SNEC models and other semi-analytic calculations, concerning both SNe II-P and IIb, can be found in Nagy & Vinkó (2016).

The parameters derived from the modelling of the quasi-bolometric light curve of SN 2013df near peak are listed in Table 6. The values shown in the second and third columns pertain to the He-rich core and the outer shell assumed to consist of a mixture of H and He ($\kappa = 0.3$ cm^2 g^{-1}), respectively. We also show the results originating from the best-fitting model using a pure H-shell ($\kappa = 0.4$ cm^2 g^{-1}). As mentioned above, these two cases result in very similar parameter sets.

In the following, we discuss three important details. First, it is not possible to derive the independent values of the opacity, the ejected mass ($M_{\rm ej}$) and the kinetic energy ($E_{\rm kin}$) by this method. Instead, only the degenerate combinations of $M_{\rm ej}\kappa$ or $E_{\rm kin}\kappa$ can be constrained by the observations (see WJC15 for details). This needs to be taken into account if one compares the values for the ejecta masses and kinetic energies originating from various sources. Thus, for example, the $M_{\rm ej}$ and $E_{\rm kin}$ values concerning the He-rich core need to be expressed as $(M_{\rm ej}\kappa)/(0.2$ cm^2 g$^{-1})$ and $(E_{\rm kin}\kappa)/(0.2$ cm^2 g$^{-1})$, respectively (as noted in Table 6). Using $\kappa = 0.2$ cm^2 g^{-1} for the optical opacity of the core, we get $M_{\rm ej} \sim 3.4$ M$_\odot$ and $E_{\rm kin} \sim 2.7 \times 10^{51}$ erg. Varying the values of κ in a range of 0.10–0.24 cm^2 g^{-1} results in masses between 3.2 and 4.6 M$_\odot$ and kinetic energies of $\sim$2.6–2.8 $\times 10^{51}$ erg. For the best-fitting models, the initial radius of the core, $R_{0,\,\rm core}$, and the initial thermal energy, $E_{\rm Th}$, also varied between 5–8 $\times 10^{11}$ cm and 2.3–2.6 $\times 10^{51}$ erg, respectively.

Secondly, the $M_{\rm ej}$ and $E_{\rm kin}$ values concerning stripped envelope SNe can be very different, depending if they are determined from the modelling of the peak or the tail of the light curve (WJC15). This problem will be discussed in Section 4.3.

Thirdly, it is worth comparing our results to the previously published ones. MG14 also presented a light-curve analysis based on the method of Arnett (1982); however, their parameter set is quite different from ours. As discussed in Section 4.1, MG14 used a larger value for the distance than we did, which leads to systematic differences in the absolute magnitudes and luminosities. These differences obviously lead to different initial nickel masses ($M_{\rm Ni} \sim 0.04$ M$_\odot$ versus $\sim$0.10–0.13 M$_\odot$ determined by MG14).

There are also relatively large differences between our values and those of MG14 concerning the ejecta mass ($\sim$3.4 M$_\odot$ versus 0.8–1.4 M$_\odot$) and the initial kinetic energy ($\sim 2.7 \times 10^{51}$ erg versus 0.4–1.2 $\times 10^{51}$ erg). We suggest that the main reason of these differences connects to the time-scales. Based on the model of Arnett (1982), $M_{\rm ej}$ and $E_{\rm kin}$ can be determined from two peak parameters, the characteristic ejecta velocity, $v_{\rm sc}$, and the rise time, $t_{\rm rise}$ (see e.g. WJC15):

$$\text{(a)}\quad M_{\rm ej} = \frac{1}{2}\frac{\beta c}{\kappa} v_{\rm sc} t_{\rm rise}^2, \quad \text{(b)}\quad E_{\rm kin} = \frac{3}{20}\frac{\beta c}{\kappa} v_{\rm sc}^3 t_{\rm rise}^2, \qquad (2)$$

where $\beta = 13.8$ is an integration constant, c is the speed of light. $t_{\rm rise}$ is assumed to be equivalent with the mean light-curve time-scale, $\tau_{\rm m} = \sqrt{2\tau_{\rm d}\tau_{\rm h}}$, where $\tau_{\rm d}$ is the diffusion time-scale and $\tau_{\rm h} = R_0/v_{\rm sc}$ is the hydrodynamic time-scale, respectively. Nevertheless, these assumptions of the Arnett model are valid only in that case when R_0 is negligible, which is not true for SNe having extended progenitors, i.e. for SNe II-P or eIIb. For SN 2013df, we derived $R_0 = 7.4 \times 10^{11}$ cm ($\sim$11 R$_\odot$) for the He-rich core. In this case, the contribution of the initial thermal energy ($E_{\rm th}$, deposited by the shock) to the light curve is significant (see Table 6). One needs

[6] http://mesa.sourceforge.net
[7] http://stellarcollapse.org/snec

Table 6. Log of parameters derived from bolometric light-curve modelling.

Parameter	Core (He-rich) ($\kappa = 0.2$ cm^2 g^{-1})	Shell (mixed H-He) ($\kappa = 0.3$ cm^2 g^{-1})	Shell (pure H) ($\kappa = 0.4$ cm^2 g^{-1})	Remarks
R_0 (cm)	7.4×10^{11}	1.1×10^{13}	1.2×10^{13}	Initial radius of the ejecta
$T_{\rm rec}$ (K)	10 000[a]	–	–	Recombination temperature
$M_{\rm ej}$ ($M_\odot$)	3.38[b]	0.08[b]	0.065[b]	Ejecta mass
$M_{\rm Ni}$ ($M_\odot$)	0.043	–	–	Initial nickel mass
$E_{\rm Th}$ (foe)	2.45	0.25	0.25	Initial thermal energy
$E_{\rm kin}$ (foe)	2.7[b]	0.2[b]	0.2[b]	Initial kinetic energy

Notes. [a]Adopted from Hatano et al. (1999).
[b]Because of the $M_{\rm ej}\kappa$ and $E_{\rm kin}\kappa$ degeneracies, the $M_{\rm ej}$ and $E_{\rm kin}$ values given here are scaled to the opacities shown in the header.

to take into account that the shock-heated ejecta also radiates, and that modifies the light-curve shape considerably. Recombination is also a major process that can significantly affect the measured peak time of the light curve (Arnett & Fu 1989; Nagy & Vinkó 2016). All of these details must be considered in modelling the light curves of Type II SNe. Otherwise, the naive estimation of $t_{\rm rise} = \tau_{\rm m}$ may lead to the significant underestimation of $M_{\rm ej}$ and $E_{\rm kin}$. For example, if we calculate $\tau_{\rm m}$ from the best-fitting model parameters listed in Table 6, we get 27.5 d, which is much larger than the observed rise time estimated to be ∼22 d.

We also note that there is a typo in Arnett (1982) where the relation between the photospheric velocity, the kinetic energy and the ejecta mass is given as $v^2_{\rm phot} = 3/5(2E_{\rm kin}/M_{\rm ej})$, as recently pointed out by WJC15. This typo was corrected in Arnett (1996) where the proper relation was given as $v^2_{\rm phot} = 5/3(2E_{\rm kin}/M_{\rm ej})$, but this error has propagated in the literature, for example into Valenti et al. (2008) whose formulae were applied by MG14.

Our two-component model allowed us to extract information on the parameters of the outer shell including the initial radius of the extended H-rich material, $R_{0,\,\rm shell}$; however, we note that determination of this parameter is very uncertain, especially, if the light curve is not well sampled in the initial declining phase. Thus, we consider the value of $R_{0,\,\rm shell} \sim 1.1$–$1.2 \times 10^{13}$ cm (∼160–170 $R_\odot$) as a lower limit. This conclusion does not contradict the results of VD14 who determined $R_{\rm eff} = 545 \pm 65$ $R_\odot$ as the effective radius of the progenitor based on *HST* images obtained 14 yr before explosion. Since the model applied by MG14 cannot be used for fitting the very early part of the bolometric light curve (i.e. the epochs before the secondary maximum), they could not estimate the shell parameters this way. Instead, they used the formulae of Nakar & Piro (2014) to constrain the mass and the radius of the shell. As they noted, this method also produces very uncertain results if there are no observed data in the very early phases of the light curve, or only in one filter (which is true for SN 2013df). Therefore, they also defined the value of the radius of the extended material of $R_{\rm ext} \sim 64$–169 $R_\odot$, which should be considered as a lower limit, while lacking the observed peak luminosity of the shock breakout.

4.3 Explosion parameters from late-time photometry

Based on the method of Arnett (1982), the properties of the late-time light curves can be predicted from the physical parameters inferred from the early part of the light curves of stripped envelope SNe. The observed late-time light curves may vary substantially for SN Ib, Ic and IIb despite their similar early-time light curves (see Clocchiatti & Wheeler 1997; Wheeler et al. 2015). The differences of the late-time light curve behaviour are indicative of heterogeneous explosion kinematics and progenitor masses concerning this type of stellar explosions. WJC15 suggested that there may be a discrepancy between the fitted tail decay parameters and those obtained from the fit to the rising part of the light curve. That suggest incomplete physical modelling of the whole light curve.

Here, we address the issue of deriving physical parameters from the light-curve tail of SN 2013df, and compare late-time results to those obtained from the peak properties. We used three data sets, which all consist of measurements obtained after +50 d, to construct the late-time light curve. Our unfiltered ROTSE observations cover the epochs between +50 and +82 d, and also contain a single measurement obtained at +168 d (note that some of these data have quite high uncertainties). Additionally, we adopted the late-time r'-band data of MG14 that extend up to +252 d. These late-time data show significant epoch-to-epoch variations around an exponential decline of ∼0.019 mag d^{-1}. We also included one R band and three r'-band photometric points (obtained at +199, +262, +298, and +348 d, respectively) published by Maeda et al. (2015); we converted the R-band magnitude belonging to +199 d into an r'-band value using the calibration by Jordi, Grebel & Ammon (2006). Following the description of Lyman, Bersier & James (2014) and WJC15, we neglected the bolometric corrections and assumed that these late-time photometric values are proxies of the bolometric luminosities to within a constant scaling factor. As earlier, we used $t_0 = 2456\,447.8 \pm 0.5$ JD and $\mu_0 = 31.10 \pm 0.05$ mag while deriving the luminosities.

The late-time light curve of stripped envelope SNe is thought to be powered by the energy input from the decay of ^{56}Ni and ^{56}Co, mainly via the thermalization of the emerging γ-ray photons trapped in the expanding material (see e.g. Cappellaro et al. 1997; Vinkó et al. 2004, as well as WJC15, and references therein). Depending on the density of the ejecta, part of the high-energy photons leak out from the ejecta; the degree of γ-ray leakage is indicated by the steepness of the late-time light curve. A fraction of the decay energy leads to the production of positrons, which are slowed down and annihilated by the ejecta material.

The rate of energy production in γ-rays can be given as

$$E_\gamma = M_{\rm Ni}\left[\epsilon_{\rm Ni}\,{\rm e}^{-t/\tau_{\rm Ni}} + \epsilon_{\rm Co}\left({\rm e}^{-t/\tau_{\rm Co}} - {\rm e}^{-t/\tau_{\rm Ni}}\right)\right], \quad (3)$$

where $M_{\rm Ni}$ is the mass of the synthesized nickel, $\epsilon_{\rm Ni} = 3.9 \times 10^{10}$ erg s^{-1} g^{-1} and $\epsilon_{\rm Co} = 6.8 \times 10^9$ erg s^{-1} g^{-1} are the energy generation rates of ^{56}Ni and ^{56}Co, respectively (see e.g. Nadyozhin 1994; Arnett 1996), while $\tau_{\rm Ni} = 8.8$ d and $\tau_{\rm Co} = 111.3$ d are the decay times of ^{56}Ni and ^{56}Co, respectively. The total radiated luminosity resulting from the γ-ray trapping per seconds can be approximated as

$$L_\gamma = E_\gamma\, D_\gamma = E_\gamma\left(1 - {\rm e}^{-(T_0/t)^2}\right), \quad (4)$$

where D_γ is the γ-ray deposition function and T_0 is defined as the characteristic time-scale for the leakage of γ-rays.

Following Branch & Wheeler (2016), we describe the rate of energy production due to positrons as

$$E_+ = M_{\rm Ni}\left[\left(\epsilon_{\rm kin} + \epsilon_{\rm an}\ D_\gamma\right)\ \left(\mathrm{e}^{-t/\tau_{\rm Co}}\ -\ \mathrm{e}^{-t/\tau_{\rm Ni}}\right)\right], \quad (5)$$

where $\epsilon_{\rm kin} = 2.18 \times 10^8$ erg s^{-1} g^{-1} and $\epsilon_{\rm an} = 3.63 \times 10^8$ erg s^{-1} g^{-1} are the energy generation rates of the thermalization and the annihilation of positrons, respectively (calculated from Nadyozhin 1994). Using a similar approximation for positron trapping as for the γ-rays, the total radiated power of positrons is given by the following formula:

$$L_+ = E_+\ D_+\ = E_+\ \left(1\ -\ \mathrm{e}^{-(T_+/t)^2}\right), \quad (6)$$

where T_+ is defined as the characteristic time-scale for the leakage of positrons. Note that the positron deposition involves two deposition functions. One, D_+, is intrinsic to the transport and trapping of the positrons and treated here as if there were an effective positron transport opacity. The other is the deposition function that also applies to γ-rays, D_γ. The annihilation term involves a product of both deposition functions since the positrons must be stopped before they can annihilate, and the resulting γ-rays are then subject to (approximately) the same deposition function as the γ-rays produced directly in the decay.

The total late-time luminosity thus becomes the sum of the γ-ray and positron energy production,

$$L = L_\gamma\ +\ L_+\,. \quad (7)$$

While the deposition of positrons is often neglected or treated crudely (see e.g. WJC15 and references therein), we tried to handle them explicitly to examine their effect on the determination of the explosion parameters (as was done with various approximations by e.g. Cappellaro et al. 1997; Vinkó et al. 2004; Valenti et al. 2008). First, we assumed that the late-time light curve can be described using only one characteristic time-scale, which yielded $T_0 = T_+ = 135 \pm 5$ d. While this value may be realistic for the time-scale of γ-ray leakage, it is too short for the time-scale of positron leakage. We thus adopted different time-scales for the γ-ray and positron depositions. Following Clocchiatti & Wheeler (1997), we specified these time-scales assuming constant density as

$$\text{(a)}\quad T_0 = \sqrt{\frac{3\ \kappa_\gamma\ M_{\rm ej}}{4\pi\ v_{\rm phot}^2}}, \quad \text{and} \quad \text{(b)}\quad T_+ = \sqrt{\frac{3\ \kappa_+\ M_{\rm ej}}{4\pi\ v_{\rm phot}^2}}, \quad (8)$$

where $v_{\rm phot}$ is the photospheric velocity at the peak, $\kappa_\gamma \approx 0.027$–$0.030$ cm^2 g^{-1} (Colgate, Petschek & Kriese 1980) and $\kappa_+ \approx$ 7–10 cm^2 g^{-1} are the typical opacities of γ-rays and positrons, respectively (Colgate, Petschek & Kriese 1980; Milne, The & Laising 1999; Penney & Höflich 2014). We note that the value of κ_+ is quite uncertain. In all the cited papers, the transport of positrons and γ-rays were modelled in SN Ia atmospheres; the results, based on Monte Carlo simulations, imply that not only the degree of ionization but also the strength of the magnetic field need to be taken into account to give the exact value of κ_+.

In the lack of other information concerning SN IIb atmospheres, we chose $\kappa_+ = 7$ cm^2 g^{-1} and $\kappa_\gamma = 0.028$ cm^2 g^{-1} for our further investigations. Using these values, the relations given in equation (8) imply that $T_+/T_0 = \sqrt{\kappa_+/\kappa_\gamma} \approx 15.8$. Taking this condition into account, the second fit to the late-time light curve yielded $T_0 = 95 \pm 1$ d and $T_+ = 1500 \pm 15.8$ d. This large value of T_+ seems to be consistent with the commonly accepted hypothesis that positrons are almost completely trapped in the ejecta, but a fraction of them might escape (see e.g. Clocchiatti & Wheeler 1997). The best-fitting model to the late-time light curve, described by equation (7) and applying the boundary condition for T_+ discussed above, is shown in Fig. 11. The smaller value of T_0 is closer to the values predicted from the peak by WJC15.

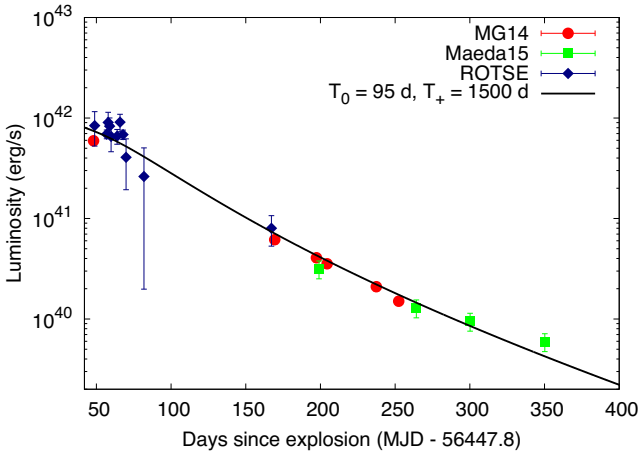

Figure 11. The best-fitting model curve described by equation (7) to the late-time light curve of SN 2013df, which was calculated from our ROTSE data (diamonds), as well as from the late-time r'-band measurements of MG14 (with circles) and Maeda et al. (2015, rectangles). See details in the text.

Using the characteristic time-scales determined from the second fit, and $v_{\rm phot} = 9000$ km s^{-1} for the photospheric velocity at the secondary maximum (see Table 3), we derived the ejecta mass of $M_{\rm ej} = 3.75$–4.20 M$_\odot$ from equation (8a); the lowest and the highest value of $M_{\rm ej}$ belongs to $\kappa_\gamma = 0.030$ and 0.027, respectively. From the values of T_0 and $M_{\rm ej}$ determined from the second fit, the kinetic energy can be calculated as

$$E_{\rm kin} = (9\kappa_\gamma M_{\rm ej}^2)/(40\pi T_0^2), \quad (9)$$

which gives $E_{\rm kin} = 1.56$–2.30×10^{51} erg.

The values of the ejecta mass and the kinetic energy originating from the analysis of the late-time light curve employing separate time-scales for the γ-ray and positron deposition agree well with those determined from the modelling of the early-time bolometric light curve (see Section 4.2). If we had used the T_0 value from the first fit of the late-time light curve (where we assumed the same time-scale for the leakage of γ-rays and positrons), we would get a factor of $\sim$2 larger ejecta mass. This implies that the correct handling of the positron deposition functions may play an important role in the determination of the explosion parameters via the analysis of light-curve tails of stripped envelope SNe.

WJC15 found significant inconsistencies in the ejecta masses (as well as in the kinetic energies) originating from the analysis of the peak and of the tail of the light curves. They suggested that those inconsistencies could be resolved by assuming very small optical opacities ($\kappa \sim 0.01$–0.1 g cm^{-2}) in the ejecta around the maximum (the very low values of κ in the ejecta of stripped envelope SNe were also assumed by e.g. Ensman & Woosley 1988; Kleiser & Kasen 2014). In the case of SN 2013df, there are two steps seem to be important in solving this problem. First, we developed a model, in which $M_{\rm ej}$ and $E_{\rm kin}$ are input parameters, thus they can be directly determined from the fitting. This allowed us to avoid to calculate these parameters from the rise time to the secondary peak, which is usually assumed to have an exact physical meaning ($t_{\rm rise} = \tau_{\rm m} = \sqrt{2\tau_{\rm d}\tau_{\rm h}}$), but which is only true in the cases of compact progenitors.

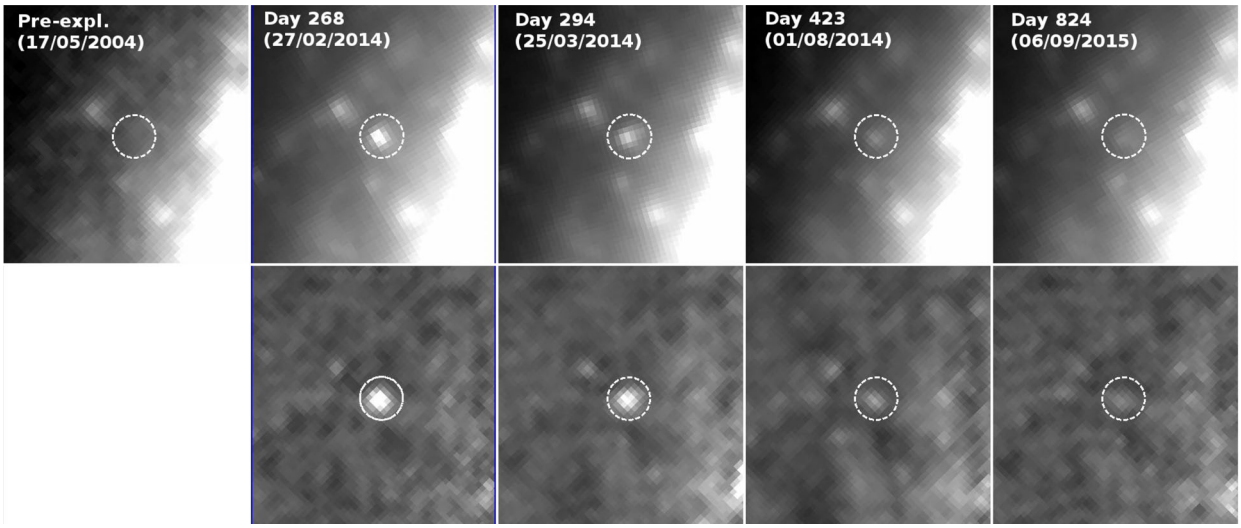

Figure 12. The mid-IR evolution of SN 2013df on *Spitzer* 4.5 μm images (top: original PBCD images, bottom: background-subtracted images).

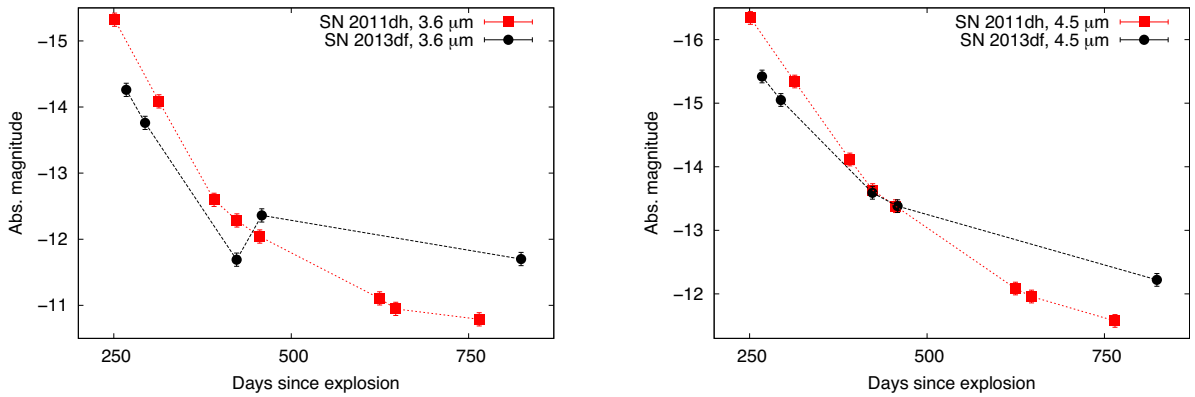

Figure 13. Late-time 3.6 (left-hand panel) and 4.5 micron (right-hand panel) light curves of SNe 2011dh (Ergon et al. 2015, filled rectangles) and 2013df (Tinyanont et al. 2016, filled circles). Absolute magnitudes were calculated using the distances of $D = 8.4$ and 16.6 Mpc, respectively.

Secondly, we tried to handle explicitly the effects of the deposition of γ-rays and positrons during the analysis of the light-curve tail.

Nevertheless, there are several other theoretical and observational aspects that need to be taken into account, and the findings concerning SN 2013df do not necessarily help to answer the open questions concerning other SN IIb, or, even more, SN Ib/c. Both the peak and tail models contain simplifications and uncertainties, whose effects on the parameter sets are not exactly known. Moreover, the photometric errors or the lack of multicolour observations concerning the late-time data, the uncertainties of some observational parameters (especially those of t_0 and $v_{\rm phot}$), as well as the systematic uncertainties of μ_0 may also significantly affect the inferred explosion parameters. As WJC15 also noted, these problems only can be solved via careful analyses of homogeneous, high-quality multicolour data that cover both the peak and the tail of the light-curves well.

4.4 Signs of CSM interaction from late-time *Spitzer* photometry

In addition to the analysis based on our optical spectroscopic and photometric data, we also studied the late-time mid-IR data of SN 2013df. Up to now, SN 2011dh was the only SN IIb with published late-time mid-IR fluxes (Helou et al. 2013; Ergon et al. 2014, 2015). Very recently, Tinyanont et al. (2016) published the results of the SPIRITS (SPitzer InfraRed Intensive Transients Survey, PI: Kasliwal) programme, during that they monitored several nearby galaxies (and transients in them) in the near past with the Infrared Array Camera (IRAC) of the *Spitzer Space Telescope*. This data set includes measurements about the host galaxy of SN 2013df obtained at five epochs between +264 and +824 d.

Although the detailed analysis of the *Spitzer* data of SN 2013df is beyond the scope of this paper, the study of the mid-IR light curves offers a good chance to look into the late-time evolution of the SN. As it can be seen in Fig. 12, the object is clearly detectable in mid-IR even more than 2 yr after explosion (for the better visibility, we also present background-subtracted images created with HOTPANTS,[8] using a set of pre-explosion IRAC images obtained in 2004 by Fazio et al. as templates).

Fig. 13 shows the comparison of late-time mid-IR light curves of SN 2013df (Tinyanont et al. 2016) and those of SN 2011dh (Ergon et al. 2015). We scaled the *Spitzer* fluxes of SN 2011dh to the distance of SN 2013df ($D = 16.6$ Mpc), adopting $D = 8.4$ Mpc for the distance of SN 2011dh (Marion et al. 2014). While the mid-IR

[8] http://www.astro.washington.edu/users/becker/hotpants.html; developed by A. Becker.

evolution of the two objects seem to be similar between ∼250 and 350 d (in this period, SN 2011dh seems to be even brighter than SN 2013df), none of the 3.6 and 4.5 μm light curves of SN 2013df follow the drop of those of SN 2011dh after +350 d (moreover, SN 2013df seems to show a rebrightening at 3.6 μm).

Helou et al. (2013) found that the late-time mid-IR behaviour of SN 2011dh cannot be explained by a simple thermal echo model but only with additional dust heating or line emission mechanisms. Therefore, the source of the more slower decreasing late-time mid-IR excess of SN 2013df must represent an even larger amount of dust formed in the ejecta (see e.g. Kozasa et al. 2009; Nozawa et al. 2010) or formed/heated during the interaction of the ejecta and the surrounding circumstellar material (as has been found in SNe IIn; see Fox et al. 2011, 2013). Both processes can take place in SN IIb some hundreds of days after explosion (see Gall, Hjorth & Andersen 2011, for a review).

This finding is consistent with the results of Maeda et al. (2015) who found signs of strong CSM interaction (emergence of broad and flat-topped Hα and He I emission lines), beginning at ∼1 yr after explosion, in the late-time optical spectra of SN 2013df. Very similar effect was found in the case of the well-known interacting SN IIb 1993J (Matheson et al. 2000, 2001), while there was only a marginal detection of a broad Hα line in the late spectra of SN 2011dh (see Shivvers et al. 2013; Maeda et al. 2015). Late-time radio and X-ray behaviour of SN 2013df is also very similar to that of SN 1993J, indicating also ongoing CSM interaction (see Kamble et al. 2016, and references therein).

The late-time CSM interaction may also affect the optical light-curve tail of SN 2013df. As seen in Fig. 11, the last point at ∼350 d is well above the best-fitting model. This effect can be explained with the emergence of the strong Hα emission, which seems to appear as an excess in the r'-band flux.

5 CONCLUSIONS

According to previous results, we found SN 2013df to be an extended SN IIb, showing a close spectral similarity with SN 1993J. While the light-curve evolutions of the two SNe are also similar, SN 2013df seems to be less luminous than SN 1993J (but there are relatively large uncertainties concerning the distance of the host galaxy of SN 2013df). The application of the SYNAPPS spectral synthesis code allowed us to determine some important physical parameters of the ejecta: we found a continuously decreasing photospheric temperature from 8000 to 5800 K, and a decreasing photospheric velocity from ∼14 000 to 8000 km s^{-1} between +9 and +34 d. While the temperatures are consistent with the ones published by MG14 and BA15, the photospheric velocities are significantly larger than those previously reported concerning SN 2013df. The exact determination of the photospheric velocity at the secondary peak is specifically important, because it is used as an input parameter in the calculation of the ejecta mass and the initial kinetic energy via fitting the light-curve tail.

Our most important result concerning the spectral analysis is the identification of 'HV' He I features in the early spectra. At +9 and +12 d, the He I λ5876 profile could be fit with a single He I line at $v \sim 14\,000$ km s^{-1}. A lower velocity component at $v \sim 7800$ km s^{-1} appears after +19 d. Similar but less conspicuous HV feature are also seen in the He I λ6678 line. Similar spectral properties are seen in the cases of SNe 1993J and 2011fu, both of which belong also to SN eIIb. On the other hand, the spectra of several other SN IIb, which are thought to emerge from more compact progenitors, do not show this effect. Moreover, while most SN IIb can be characterized by a clear separation of H and He lines in velocity space (∼4–5000 km s^{-1}), such a separation is not seen in the case of either SNe 2013df, 1993J or 2011fu, as well as in the light echo spectra of Cas A (which all thought to emerge from extended progenitors). These findings indicate that the early 'HV' He features might form in the low-mass H-rich envelope on top of the denser, He-rich core. The evolution of the He lines can be described by the inward motion of the photosphere from the HV outer envelope to the more slowly expanding core. The presence of this effect may depend on the degree of the mixing of H and He layers, which may be more significant in extended supergiant stars than in more compact progenitors (e.g. Wolf–Rayet stars). This is a possible explanation why we only see this non-separation of Hα and He I λ5876 velocities in the cases of SN eIIb. Nevertheless, further studies are necessary to reveal the currently unknown details of this effect, which may require even more sophisticated tools e.g. Monte Carlo radiative transfer codes.

We fitted a semi-analytic model to the early bolometric light curve of SN 2013df. The derived explosion parameters are consistent with those of other SN IIb (taking into account the uncertainties concerning the distances). We found a lower limit of the initial radius of the ejecta of ∼160 $R_\odot$, which is consistent with the result of MG14, and does not contradict the progenitor radius $R_{\rm eff} \sim 545$ $R_\odot$ estimated by VD14. The analysis of the late-time light curve decline, taking into account the leakage of both the γ-rays and positrons originating from the ^{56}Co-decay, resulted in an ejecta mass (3.7–4.2 $M_\odot$) and kinetic energy (1.6–2.3 × 10^{51} erg) that are in good agreement with the same parameters estimated from fitting the secondary peak of the light curve (3.2–4.6 $M_\odot$ and 2.6–2.8 × 10^{51} erg, respectively). This finding seems to contradict the general discrepancy, found by WJC15, concerning the ejecta masses end kinetic energies inferred from the early- and late-time light curves of stripped envelope SNe. We suggest that there are two key steps in our analysis that allowed us to find seemingly consistent solutions for $M_{\rm ej}$ and $E_{\rm kin}$ in the case of SN 2013df: first, the careful handling of time-scales and relations originating from Arnett's model during the analysis of the light-curve peak, and, secondly, the explicit handling of positron deposition during the light-curve tail fitting. On the other hand, it should be kept in mind that the models we applied for the spectrum synthesis and for the light-curve fitting have limitations and caveats. For example, beside the effect of the constant opacity, as discussed in Nagy & Vinkó (2016), the light-curve model is clearly affected by the assumption of the centrally peaked distribution of ^{56}Ni. There are more complex modelling codes available, like SNEC (Morozova et al. 2015) or TARDIS (Kerzendorf & Sim 2014), which, when fully developed, will be promising future improvements to the simple calculations presented in this paper. Nevertheless, there are a lot of open questions concerning the determination of the explosion parameters of stripped envelope SNe; in order to find the answers to them, well-sampled data sets need to be obtained, which should be carefully analysed applying either analytic or hydrodynamic codes.

We also studied late-time mid-IR data obtained with *Spitzer*. Both the 3.6 and 4.5 μm light curves of SN 2013df show an excess to those of SN 2011dh between ∼+350 and +825 d. This indicates circumstellar interaction starting ∼1 yr after explosion, in accordance with previously published optical, X-ray, and radio data.

ACKNOWLEDGEMENTS

This work has been supported by the Hungarian Scientific Research Fund (OTKA) Grants NN107637, K104607, K83790, and

K113117. TS is supported by the OTKA Postdoctoral Fellowship PD112325. JCW's Supernova group at the UT Austin is supported by NSF Grant AST 11-09881 grant. JMS is supported by an NSF Astronomy and Astrophysics Postdoctoral Fellowship under award AST-1302771. KS and AP are supported by the 'Lendület-2009' Young Researchers Program and the LP2012-31 grant of the Hungarian Academy of Sciences, respectively; KS is also supported by the ESA PECS Contract no. 4000110889/14/NL/NDe.

The HET is a joint project of the University of Texas at Austin, the Pennsylvania State University, Stanford University, Ludwig-Maximilians-Universität München, and Georg-August-Universität Göttingen. The HET is named in honor of its principal benefactors, William P. Hobby and Robert E. Eberly. The Marcario Low Resolution Spectrograph is named for Mike Marcario of High Lonesome Optics who fabricated several optics for the instrument but died before its completion. The LRS is a joint project of the HET partnership and the Instituto de Astronomía de la Universidad Nacional Autónoma de México. We acknowledge the thorough work of the HET resident astronomers, Matthew Shetrone, Stephen Odewahn, John Caldwell and Sergey Rostopchin during the acquisition of the spectra.

ROTSE IIIb telescope operation and data analysis is supported by NASA grant NNX10A196H (P.I. Kehoe).

This research has made use of the NED which is operated by the Jet Propulsion Laboratory, California Institute of Technology, under contract with the National Aeronautics and Space Administration. We acknowledge the availability of NASA ADS services.

REFERENCES

Arcavi I. et al., 2011, ApJ, 742, L7
Arnett W. D., 1982, ApJ, 253, 785
Arnett W. D., 1996, Supernovae and Nucleosynthesis: An Investigation of the History of Matter, from the Big Bang to the Present. Princeton Univ. Press, Princeton, NJ
Arnett W. D., Fu A., 1989, ApJ, 340, 396
Barbon R., Benetti S., Cappellaro E., Patat F., Turatto M., Iijima T., 1995, A&AS, 110, 513
Ben-Ami S. et al., 2015, ApJ, 803, 40 (BA15)
Benvenuto O. G., Bersten M. C., Nomoto K., 2013, ApJ, 762, 74
Bersten M. C. et al., 2012, ApJ, 757, 31
Bessell M. S., Castelli F., Plez B., 1998, A&A, 333, 231
Branch D., 2001, in Livio M., ed., Supernovae and Gamma-Ray Bursts: the Greatest Explosions Since the Big Bang. Cambridge Univ. Press, Cambridge, p. 96
Branch D., Wheeler J. C., 2016, Supernovae. Springer-Verlag, Berlin
Branch D. et al., 2002, ApJ, 566, 1005
Breeveld A. A., Landsman W., Holland S. T., Roming P., Kuin N. P. M., Page M. J., 2011, in McEnery J. E., Racusin J. L., Gehrels N., eds, AIP Conf. Proc. Vol. 1358, Gamma Ray Bursts 2010. Am. Inst. Phys., New York, p. 373
Bufano F. et al., 2014, MNRAS, 439, 1807
Cano Z., 2013, MNRAS, 434, 1098
Capellaro E., Mazzali P. A., Benetti S., Danziger I. J., Turatto M., della Valle M., Patat F., 1997, A&A, 328, 203
Cenko S. B., Clubb K. I., Zheng W., Kelly P. L., Filippenko A. V., Van Dyk S. D., 2013, Cent. Bur. Electron. Telegrams, 3557, 1
Chatzopoulos E., Wheeler J. C., Vinkó J., 2012, ApJ, 746, 121
Chevalier R. A., Fransson C., 2008, ApJ, 683, L135
Chevalier R. A., Soderberg A. M., 2010, ApJ, 711, L40
Chornock R. et al., 2011, ApJ, 739, 41
Ciabattari F., Mazzoni E., Donati S., Petroni G., Foglia S., Galli G., 2013, Cent. Bur. Electron. Telegrams, 3557, 1
Claeys J. S. W., de Mink S. E., Pols O. R., Eldridge J. J., Baes M., 2011, A&A, 528, 131
Clocchiatti A., Wheeler J. C., 1997, ApJ, 491, 375
Colgate S. A., Petschek A. G., Kriese J. T., 1980, ApJ, 237, L81
Crockett R. M. et al., 2008, MNRAS, 391, L5
Cushing M. C., Vacca W. D., Rayner J. T., 2004, PASP, 116, 362
DeLaney T. et al., 2010, ApJ, 725, 2038
Dessart L., Hillier D. J., Livne E., Yoon S-C., Woosley S., Waldman R., Langer N., 2011, MNRAS, 414, 2985
Elmhamdi A., Danziger I. J., Branch D., Leibundgut B., Baron E., Kirshner R. P., 2006, A&A, 450, 305
Ensman L. M., Woosley S. E., 1988, ApJ, 333, 754
Ergon M. et al., 2014, A&A, 562, 35
Ergon M. et al., 2015, A&A, 580, 142
Fesen R. A., Milisavljevic D., 2016, ApJ, 818, 17
Filippenko A. V., 1988, AJ, 96, 1941
Filippenko A. V., Matheson T., Ho L. C., 1993, ApJ, 415, L103
Fitzpatrick E. L., Massa D., 2007, ApJ, 663, 320
Folatelli G. et al., 2006, ApJ, 641, 1039
Folatelli G. et al., 2014, ApJ, 792, 7
Folatelli G., Bersten M. C., Kuncarayakti H., Benvenuto O. G., Maeda K., Nomoto K., 2015, ApJ, 811, 147
Fox O. D. et al., 2011, ApJ, 741, 7
Fox O. D., Filippenko A. V., Skrutskie M. F., Silverman J. M., Ganeshalingam M., Cenko S. B., Clubb K. I., 2013, AJ, 146, 2
Fox O. D. et al., 2014, ApJ, 790, 17
Freedman W. L. et al., 2001, ApJ, 553, 47
Gal-Yam A. et al., 2014, Nature, 509, 471
Gall C., Hjorth J., Andersen A. C., 2011, A&AR, 19, 43
Hachinger S., Mazzali P. A., Taubenberger S., Hillebrandt W., Nomoto K., Sauer D. N., 2012, MNRAS, 422, 70
Hamuy M. et al., 2009, ApJ, 703, 1612
Hatano K., Branch D., Fisher A., Millard J., Baron E., 1999, ApJS, 121, 233
Helou G., Kasliwal M. M., Ofek E. O., Arcavi I., Surace J., Gal-Yam A., 2013, ApJ, 778, L19
Höflich P., 1995, ApJ, 440, 821
Höflich P., Wheeler J. C., Hines D. C., Trammell S. R., 1996, ApJ, 459, 307
Horesh A. et al., 2013, MNRAS, 436, 1258
Jeffery D. J., Branch D., 1990, in Wheeler J. C., Piran T., Weinberg S., eds, Supernovae, Sixth Jerusalem Winter School for Theoretical Physics. World Scientific Press, Singapore, p. 149
Jordi K., Grebel E. K., Ammon K., 2006, A&A, 460, 339
Kamble A. et al., 2016, ApJ, 818, 111
Kerzendorf W. E., Sim S. A., 2014, MNRAS, 440, 387
Kleiser I. K. W., Kasen D., 2014, MNRAS, 438, 318
Kozasa T., Nozawa T., Tominaga N., Umeda H., Maeda K., Nomoto K., 2009, in Henning T., Grün E., Steinacker J., eds, ASP Conf. Ser. Vol. 414, Cosmic Dust - Near and Far. Astron. Soc. Pac., San Francisco, p. 43
Krause O., Birkmann S. M., Usuda T., Hattori T., Goto M., Rieke G. H., Misselt K. A., 2008, Science, 320, 1195
Kumar B. et al., 2013, MNRAS, 431, 308
Landolt A. U., 1992, AJ, 104, 340
Langer N., 2012, ARA&A, 50, 107
Lewis J. R. et al., 1994, MNRAS, 266, L27
Li W. et al., 2011, MNRAS, 412, 1441
Liu Y.-Q., Modjaz M., Bianco F. B., Graur O., 2015, preprint (arXiv:1510.08049)
Lyman J. D., Bersier D., James P. A., 2014, MNRAS, 437, 3848
Maeda K., Katsuda S., Bamba A., Terada Y., Fukazawa Y., 2014, ApJ, 785, 95
Maeda K. et al., 2015, ApJ, 807, 35
Marion G. H. et al., 2014, ApJ, 781, 69
Matheson T., Filippenko A. V., Ho L. C., Barth A. J., Leonard D. C., 2000, AJ, 120, 1499
Matheson T., Filippenko A. V., Li W., Leonard D. C., Shields J. C., 2001, AJ, 121, 1648
Mauerhan J. C. et al., 2015, MNRAS, 453, 4467
Maund J. R., Smartt S. J., 2009, Science, 324, 486
Maund J. R., Smartt S. J., Kudritzki R. P., Podsiadlowski P., Gilmore G. F., 2004, Nature, 427, 129

Maund J. R., Wheeler J. C., Patat F., Wang L., Baade D., Höflich P. A., 2007, ApJ, 671, 1944
Maund J. R. et al., 2011, ApJ, 739, L37
Mazzali P. A., Deng J., Hamuy M., Nomoto K., 2009, ApJ, 703, 1624
Milisavljevic D. et al., 2013, ApJ, 767, 71
Milne P. A., The L.-S., The, Laising M. D., 1999, ApJS, 124, 503
Modjaz M. et al., 2014, AJ, 147, 99
Morales-Garoffolo A. et al., 2014, MNRAS, 445, 1647 (MG14)
Morales-Garoffolo A. et al., 2015, MNRAS, 454, 95
Morozova V., Piro A. L., Renzo M., Ott C. D., Clausen D., Couch S. M., Ellis J., Roberts L. F., 2015, ApJ, 814, 63
Nadyozhin D. K., 1994, ApJS, 92, 527
Nagy A. P., Vinkó J., 2016, A&A, 589, A53
Nagy A. P., Ordasi A., Vinkó J., Wheeler J. C., 2014, A&A, 571, A77
Nakar E., Piro A. L., 2014, ApJ, 788, 193
Nozawa T., Kozasa T., Tominaga N., Maeda K., Umeda H., Nomoto K., Krause O., 2010, ApJ, 713, 356
Oates S. R. et al., 2012, MNRAS, 424, 1297
Pastorello A. et al., 2008, MNRAS, 389, 131
Paxton B., Bildsten L., Dotter A., Herwig F., Lesaffre P., Timmes F., 2011, ApJS, 192, 3
Paxton B. et al., 2013, ApJS, 208, 4
Penney R., Höflich P. A., 2014, ApJ, 795, 84
Qiu Y., Li W., Qiao Q., Hu J., 1999, AJ, 117, 736
Rayner J. T., Toomey D. W., Onaka P. M., Denault A. J., Stahlberger W. E., Vacca W. D., Cushing M. C., Wang S., 2003, PASP, 115, 362
Reilly E. et al., 2016, MNRAS, 457, 288
Rest A. et al., 2011, ApJ, 732, 3
Rhee M.-H., van Albada T. S., 1996, A&AS, 115, 407
Richardson D., Branch D., Baron E., 2006, AJ, 131, 2233
Richmond M. W., Treffers R. R., Filippenko A. V., Paik Y., Leibundgut B., Schulman E., Cox C. V., 1994, AJ, 107, 1022
Roming P. W. et al., 2009, ApJ, 704, 118
Sahu D K., Anupama G. C., Chakradhari N. K., 2013, MNRAS, 433, 2
Schmidt B. P. et al., 1993, Nature, 364, 600
Shivvers I. et al., 2013, MNRAS, 436, 3614
Silverman J. M., Mazzali P., Chornock R., Filippenko A. V., Clocchiatti A., Phillips M. M., Ganeshalingam M., Foley R. J., 2009, PASP, 121, 689
Silverman J. M. et al., 2012, MNRAS, 425, 1789
Taubenberger S. et al., 2011, MNRAS, 413, 2140
Thomas R. C., Nugent P. E., Meza J. C., 2011, PASP, 123, 237
Tinyanont S. et al., 2016, preprint (arXiv:1601.03440)
Trammell S. R., Hines D. C., Wheeler J. C., 1993, ApJ, 414, L21
Tran H. D., Filippenko A. V., Schmidt G. D., Bjorkman K. S., Jannuzi B. T., Smith P. S., 1997, PASP, 109, 489
Valenti S. et al., 2008, MNRAS, 383, 1485
Van Dyk S. D., Garnavich P. M., Filippenko A. V., Höflich P., Kirshner R. P., Kurucz R. L., Challis P., 2002, PASP, 114, 1322
Van Dyk S. D. et al., 2011, ApJ, 741, L28
Van Dyk S. D. et al., 2013, ApJ, 772, L32
Van Dyk S. D. et al., 2014, AJ, 147, 37 (VD14)
Vinkó J. et al., 2004, A&A, 427, 453
Vinkó J. et al., 2012, A&A, 540, A93
Wade R. A., Horne K., 1988, ApJ, 324, 411
Wheeler J. C. et al., 1993, ApJ, 417, L71
Wheeler J. C., Harkness R. P., Clocchiatti A., Benetti S., Brotherton M. S., Depoy D. L., Elias J., 1994, ApJ, 436, L135
Wheeler J. C., Johnson V., Clocchiatti A., 2015, MNRAS, 450, 1295 (WJC15)
Woosley S. E., Eastman R. G., Weaver T. A., Pinto P. A., 1994, ApJ, 429, 300
Wright E. L., 2006, PASP, 118, 1711
Yaron O., Gal-Yam A., 2012, PASP, 124, 668
Young P. A. et al., 2006, ApJ, 640, 891
Zhang Q., Hu J. Y., Wang L. F., Mazzali P. A., Wang Z. R., 1995, MNRAS, 277, 1115

APPENDIX A: PHOTOMETRIC RESULTS

Table A1. *BVRI* (Konkoly Observatory, Hungary) magnitudes of SN 2013df.

JD[a]	Phase[b] (d)	*B* (mag)	*V* (mag)	*R* (mag)	*I* (mag)
6456.4	8.6	14.78(.07)	14.51(.04)	14.41(.04)	14.19(.02)
6457.4	9.6	15.05(.07)	14.71(.02)	14.56(.04)	14.33(.01)
6458.4	10.6	15.20(.10)	14.86(.03)	14.68(.04)	14.47(.01)
6459.4	11.6	15.37(.02)	14.91(.14)	14.77(.05)	14.46(.01)
6460.4	12.6	15.41(.03)	14.92(.03)	14.67(.07)	14.49(.01)
6461.4	13.6	15.43(.03)	14.88(.04)	14.64(.04)	14.45(.02)
6462.4	14.6	15.39(.18)	14.84(.01)	14.59(.05)	14.41(.01)
6463.4	15.6	–	14.77(.01)	14.50(.02)	14.36(.02)
6464.4	16.6	15.38(.08)	14.71(.02)	14.46(.06)	14.32(.01)
6465.4	17.6	15.39(.01)	14.66(.10)	14.40(.02)	14.27(.01)
6467.4	19.6	15.40(.01)	14.57(.01)	14.30(.06)	14.19(.01)
6474.4	26.6	15.56(.16)	14.71(.01)	14.35(.03)	14.16(.12)
6475.4	27.6	15.79(.11)	14.76(.02)	14.38(.06)	14.21(.01)
6476.4	28.6	15.89(.02)	14.84(.02)	14.42(.04)	14.25(.01)
6477.4	29.6	16.12(.03)	14.95(.01)	14.50(.06)	14.30(.03)
6478.4	30.6	16.33(.02)	15.08(.02)	14.57(.02)	14.35(.02)
6480.4	32.6	16.50(.01)	15.27(.01)	14.72(.07)	14.51(.01)
6481.4	33.6	16.68(.04)	15.39(.03)	14.79(.03)	14.55(.02)
6482.4	34.6	16.87(.01)	15.49(.02)	14.83(.06)	14.59(.01)
6483.4	35.6	16.83(.01)	15.57(.01)	14.91(.05)	14.66(.03)
6485.4	37.6	16.99(.02)	15.66(.01)	15.02(.06)	14.75(.01)
6488.4	40.6	17.21(.13)	15.83(.01)	15.15(.05)	14.87(.01)
6489.4	41.6	17.19(.08)	15.83(.02)	15.18(.07)	14.85(.01)
6490.4	42.6	17.17(.09)	15.91(.01)	15.23(.06)	14.91(.02)
6491.4	43.6	17.44(.10)	15.92(.06)	15.27(.06)	14.94(.01)
6493.4	45.6	17.10(.11)	15.99(.04)	15.31(.04)	15.00(.01)

Notes. [a]JD−2450 000. [b]With respect to $t_0 = 2456\,447.8 \pm 0.5$ JD. Errors are given in parentheses.

Table A2. $g'r'i'z'$ (Baja Observatory, Hungary) magnitudes of SN 2013df.

JD[a]	Phase[b] (d)	g' (mag)	r' (mag)	i' (mag)	z' (mag)
6455.8	8.0	14.59(.03)	14.52(.02)	14.49(.03)	14.58(.04)
6456.8	9.0	14.86(.03)	14.68(.03)	14.64(.03)	14.69(.04)
6457.9	10.1	14.98(.05)	14.76(.04)	14.82(.05)	14.92(.07)
6458.8	11.0	15.09(.05)	14.83(.04)	14.82(.05)	14.72(.05)
6459.9	12.1	15.12(.03)	14.81(.02)	14.81(.03)	14.84(.04)
6460.9	13.1	15.06(.03)	14.76(.03)	14.80(.03)	14.84(.04)
6461.9	14.1	15.06(.03)	14.72(.03)	14.71(.03)	14.71(.04)
6462.9	15.1	15.01(.03)	14.60(.03)	14.64(.04)	14.75(.04)
6463.9	16.1	14.97(.04)	14.60(.03)	14.63(.04)	14.69(.04)
6464.9	17.1	15.00(.04)	14.55(.04)	14.62(.04)	14.73(.05)
6466.9	19.1	14.84(.04)	14.42(.03)	14.53(.04)	14.54(.04)
6468.9	21.1	14.91(.04)	14.33(.03)	14.49(.04)	14.69(.04)
6469.9	22.1	14.89(.03)	14.38(.02)	14.46(.03)	14.60(.04)
6470.9	23.1	14.93(.03)	14.35(.02)	14.39(.03)	14.51(.03)
6471.9	24.1	14.98(.04)	14.39(.03)	14.42(.03)	14.55(.04)
6472.9	25.1	15.05(.03)	14.40(.02)	14.49(.03)	14.55(.03)
6473.9	26.1	15.15(.02)	14.46(.02)	14.47(.03)	14.51(.03)
6474.9	27.1	15.24(.03)	14.47(.03)	14.54(.03)	14.69(.04)
6475.9	28.1	15.41(.03)	14.57(.02)	14.60(.03)	14.66(.04)
6477.9	30.1	15.61(.03)	14.71(.02)	14.70(.03)	14.73(.03)
6482.9	35.1	16.20(.06)	15.19(.05)	15.06(.06)	14.99(.07)
6483.9	36.1	16.42(.06)	15.22(.04)	15.05(.05)	15.06(.06)
6484.9	37.1	16.26(.06)	15.20(.04)	15.22(.06)	15.21(.07)
6487.9	40.1	16.60(.11)	15.29(.08)	15.20(.08)	15.03(.09)
6489.9	42.1	16.37(.10)	15.42(.07)	15.29(.08)	15.16(.09)
6490.9	43.1	16.77(.14)	15.47(.11)	15.61(.13)	15.46(.15)
6491.9	44.1	16.81(.21)	15.43(.16)	15.30(.17)	15.15(.18)

Notes. [a]JD−2450 000. [b]With respect to $t_0 = 2456\,447.8 \pm 0.5$ JD. Errors are given in parentheses.

Table A3. Unfiltered ROTSE-IIIb magnitudes of SN2013df.

MJD − 50 000	Phase[a] (d)	Magnitude
6459.2	11.9	14.88(.26)
6460.2	12.9	14.43(.36)
6461.3	14.0	14.51(.35)
6470.3	23.0	14.27(.49)
6473.2	25.9	14.01(.25)
6478.2	30.9	14.44(.13)
6479.2	31.9	14.66(.37)
6481.2	33.9	14.80(.17)
6482.2	34.9	14.66(.34)
6483.2	35.9	14.95(.07)
6484.2	36.9	14.98(.12)
6484.2	36.9	15.10(.11)
6485.2	37.9	15.46(.12)
6486.2	38.9	15.04(.21)
6487.2	39.9	15.54(.50)
6488.2	40.9	15.28(.16)
6497.2	49.9	15.45(.35)
6505.2	57.9	15.67(.10)
6506.2	58.9	15.37(.25)
6507.2	59.9	15.47(.20)
6508.2	60.9	15.72(.28)
6512.2	64.9	15.72(.17)
6514.2	66.9	15.37(.20)
6516.2	68.9	15.67(.11)
6518.2	70.9	16.24(.46)
6530.1	82.8	16.72(.71)
6615.5	168.2	18.01(.31)

Notes. [a]With respect to $t_0 = 2456\,447.8 \pm 0.5$ JD. Errors are given in parentheses.

This paper has been typeset from a TEX/LATEX file prepared by the author.